JGR Oceans

RESEARCH ARTICLE
10.1029/2022JC019015

The Effects of Ocean Surface Waves on Tropical Cyclone Intensity: Numerical Simulations Using a Regional Atmosphere-Ocean-Wave Coupled Model

Biao Zhao[1,2,3], Guansuo Wang[2,3], Jun A. Zhang[4], Li Liu[1], Jiping Liu[5], Jing Xu[6], Hao Yu[1], Chang Zhao[2,3], Xinzhu Yu[1], Chao Sun[1], and Fangli Qiao[2,3]

[1]Department of Earth System Science, Ministry of Education Key Laboratory for Earth System Modeling, Tsinghua University, Beijing, China, [2]First Institute of Oceanography, and Key Laboratory of Marine Science and Numerical Modeling, Ministry of Natural Resources, Qingdao, China, [3]Key Laboratory of Marine Science and Numerical Modeling, Shandong Province, China, [4]Hurricane Research Division, NOAA/AOML& University of Miami, Miami, FL, USA, [5]Department of Atmospheric and Environmental Sciences, State University of New York at Albany, Albany, NY, USA, [6]State Key Laboratory of Severe Weather, Chinese Academy of Meteorological Sciences, China Meteorological Administration, Beijing, China

Abstract Tropical cyclones (TCs), especially landfalling intense storms often pose serious threats to life and property in coastal areas. Although TC track forecast skill has been improved in the past decades, the progress of advancing the intensity forecast lags that of the track forecast. One possible limiting factor is the absence of ocean surface waves in forecast systems. To better represent the interaction of TC and underlying ocean, a regional atmosphere-ocean-wave coupled model is employed in this study. Twenty-one TCs of a whole year in 2013 are retrospectively simulated through twin simulations, a Control and a Fully coupled run. Results show that TC intensity bias has been significantly reduced in the fully coupled simulation, in which five ocean surface wave related physical processes are considered, including wave modulation of momentum flux, sea spray effect on enthalpy flux, surface current and Stokes drift on air sea flux, non-breaking wave induced mixing in the upper ocean as well as rain induced ocean surface cooling. A case study approach is used to diagnose the effect of individual surface wave related physical process on TC simulations. Similar to the effect of sea spray, surface waves also act as positive feedback on TC intensification by modulating air-sea momentum flux. Absolute angular momentum budget analysis suggests that larger radial inflows and stronger updrafts near the eyewall promote the radial and vertical advections of absolute angular momentum and in turn lead to a stronger TC in Fully coupled simulation. The TC structure and size agree better with observations in Fully coupled simulation.

Plain Language Summary Ocean surface waves, have been widely acknowledged to modulate the flux exchange at air-sea interface. Their influence on multiscale air-sea processes, especially tropical cyclone, has attracted much attention in recent years. However, most of the studies usually focused on TC case study. To quantify the effects of ocean surface waves on tropical cyclone evolution. This study uses a regional atmosphere-ocean-wave coupled model to conduct retrospective simulations of all 21 tropical cyclones passing through the model domain in 2013. Results show that ocean surface waves play an important role in TC intensity and structure. Surface waves enhance the simulated inflow in the boundary layer that leads to more radial momentum transport and stronger updrafts near the eyewall region. These processes together help enhance the storm intensity and reduce the biases of intensity forecasts. The findings of this research emphasize the importance of ocean surface waves for TC studies and forecasts.

Biao Zhao and Guansuo Wang contributed equally to this work.

Key Points:

- Surface waves lead to significant reduction of intensity bias and improvement of simulated TC size
- The modulation of air-sea momentum flux by surface waves acts as positive feedback on TC intensification
- The enhanced air-sea fluxes by surface waves help increase the angular momentum convergence, leading to improved representation of TC structure

Correspondence to:
F. Qiao,
qiaofl@fio.org.cn

Citation:
Zhao, B., Wang, G., Zhang, J. A., Liu, L., Liu, J., Xu, J., et al. (2022). The effects of ocean surface waves on tropical cyclone intensity: Numerical simulations using a regional atmosphere-ocean-wave coupled model. *Journal of Geophysical Research: Oceans*, *127*, e2022JC019015. https://doi.org/10.1029/2022JC019015

Received 24 JUN 2022
Accepted 31 OCT 2022

Author Contributions:
Conceptualization: Jun A. Zhang, Fangli Qiao
Formal analysis: Guansuo Wang, Hao Yu, Chang Zhao, Xinzhu Yu, Chao Sun
Methodology: Guansuo Wang, Jun A. Zhang, Li Liu, Jiping Liu, Jing Xu, Chang Zhao
Software: Li Liu, Hao Yu, Xinzhu Yu, Chao Sun
Supervision: Jun A. Zhang, Li Liu, Fangli Qiao
Validation: Guansuo Wang, Hao Yu, Chang Zhao, Chao Sun
Writing – original draft: Guansuo Wang, Jun A. Zhang, Li Liu, Jiping Liu, Fangli Qiao

1. Introduction

TC is one of the most destructive disasters in nature. TC induced heavy rain, strong winds, damaging storm surges, landslides and flooding have led to enormous economic losses in the past. Hence, accurate and reliable TC forecasts and warnings are essential to reduce those losses. In the past decades, TC track forecast skill has been continually improved, while the progress of advancing the intensity forecast lags that of the track forecast (Chen et al., 2007; DeMaria et al., 2014; Rappaport et al., 2009; Yamaguchi et al., 2017). Previous numerical studies based on coupled atmosphere-ocean simulations or forecasts from world leading agencies such as IFS of ECMWF (Mogensen et al., 2017), NHM of JMA (Wada et al., 2018), GRAPES of CMA (Yu et al., 2013), HWRF of NOAA (Bernardet et al., 2015; Mehra et al., 2018) and GFDL regional coupled model of NOAA (Bender &

Writing – review & editing: Guansuo Wang, Jun A. Zhang, Li Liu, Jiping Liu, Jing Xu, Fangli Qiao

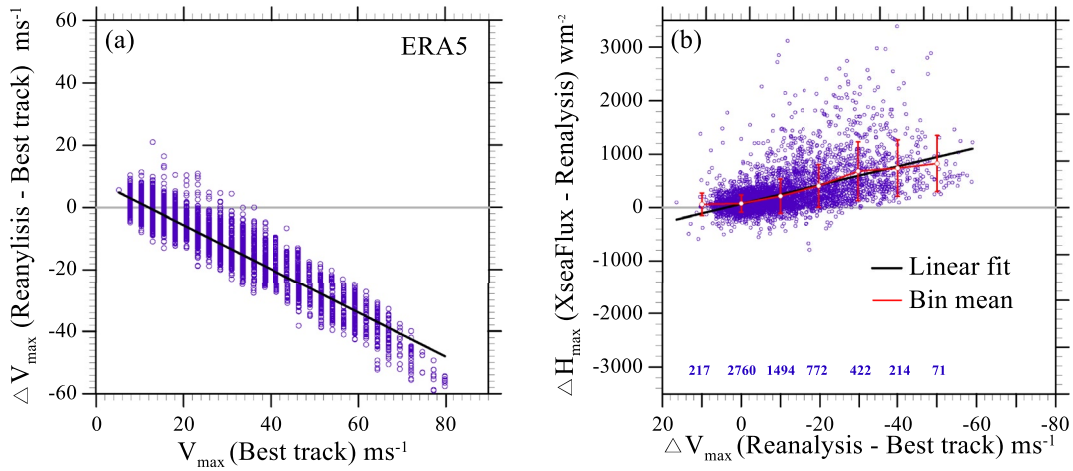

Figure 1. (a) TC intensity biases between ERA5 and best track as a function of TC intensity estimated by best track data. (b) The correlation between air-sea enthalpy flux and TC intensity. In panel (b), *y*-axis represents the differences of maximum enthalpy flux (latent plus sensible) between XseaFlux and ERA5 for all the TCs in western North Pacific during the period from 1998 to 2007. Correspondingly, the *x*-axis denotes the TC intensity biases between ERA5 reanalysis and best track. The bin size of *x*-axis is taken as 10 ms^{-1}, the red curve represents the bin-averaged enthalpy flux differences, and the bars indicate ±1 standard deviation in each bin, the linear fit is shown as black line. The sample size is also indicated in the bottom of the plot.

Ginis, 2000) have demonstrated the important role of ocean coupling in TC intensity prediction. Benefitting from an interactive ocean model and data assimilation, weak TCs in ECMWF Reanalysis version 5 (ERA5) (Hersbach et al., 2020) were well reproduced (Figure 1a). However, challenges still remain, the operational numerical models tend to underestimate strong TCs (Yamaguchi et al., 2017).

It is well known that TCs draw energy from the underlying warm ocean through exchanging air-sea enthalpy flux (Chen et al., 2007; Emanuel, 1986). By comparing simulations with measurements from the Coupled Boundary Layer Air-Sea Transfer (CBLAST) field experiment, Liu, Curry, et al. (2011) demonstrated that most of the numerical prediction reanalyses substantially underestimate the latent heat flux in hurricane conditions, while the XseaFlux data set performed much better due to the inclusion of surface wave related physical processes (i.e., wave orbital speed and breaking wave induced sea spray). The enthalpy flux differences between XseaFlux and ERA5 are highly correlated with the TC intensity bias in ERA5 (Figure 1b). Moreover, the enthalpy flux differences increase linearly with the extent of intensity underestimation, which implies that ocean surface waves may also play an important role in air-sea enthalpy flux exchange and thus TC intensity.

Ocean surface waves directly affect the air-sea flux and TC intensity. The air-sea momentum flux depends not only on wind condition but also on sea state. Using a coupled model (Warner et al., 2010), Olabarrieta et al. (2012) found that both the simulated wind velocities and wave properties agreed well with observations by considering surface wave state dependent air-sea momentum flux. Janssen (1989, 1991) pointed out that young seas have larger drag on atmosphere than that of developed seas because the young ocean waves absorb most of the wind energy. With this wave state dependent air-sea momentum flux scheme, a better wind-pressure relationship was forecasted by ECMWF operational coupled model (Bidlot et al., 2020; Magnusson et al., 2019). Dropsonde observations inside the TCs deepened the understanding of air-sea flux transfer under extreme conditions. It is found that the drag coefficient tends to saturate and levels off when the surface wind speed exceeds ~33 ms^{-1} (Powell et al., 2003). By considering the capped drag coefficient, the forecasted TC intensity was in better agreement with observations (Doyle et al., 2014; Moon et al., 2007). Under TC conditions, breaking wave induced sea spray could dramatically increase the contact area between the ocean and atmosphere, leading to more upward air-sea heat and moisture fluxes (Andreas & Emanuel, 2001; Andreas et al., 2015; Fairall et al., 2009). Numerical results suggested that TCs were strengthened by including the enthalpy effect of sea spray effect (Bao et al., 2011; Garg et al., 2018; Liu, Liu, et al., 2011; Perrie et al., 2005; Xie et al., 2010; Zweers et al., 2015). Furthermore, surface waves affect air-sea mass flux by modulating the emission of sea salt aerosol which could act as cloud condensation nuclei. It has been demonstrated that both TC track and

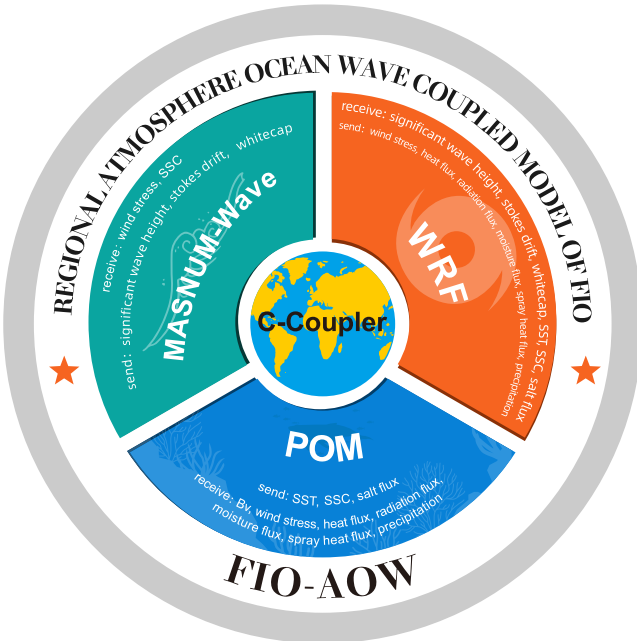

Figure 2. Framework of FIO-AOW. Variables exchanged among the component models are presented as well.

intensity are well reproduced by coupling a surface wave dependent sea salt aerosol scheme (Hoarau et al., 2018; Pianezze et al., 2018). In addition to these direct effects, surface waves may also indirectly affect TC intensity by regulating upper-ocean structure. It is well known that TC induced entrainment and upwelling bring colder water from subsurface to surface in the upper ocean (Price, 1981; Zhang et al., 2016), and the resultant cooling of sea surface temperature acts as negative feedback on TC intensity. The wave-induced mixing (Qiao et al., 2004) facilitates this negative feedback, which helps slow down TC intensification (Bruneau et al., 2018; Li et al., 2014; Zhao et al., 2017).

Although numerical studies have shown that surface waves and their related physical processes play an important role in TC modeling, most of previous studies focused on individual TC case study. Furthermore, due to limited airborne observations in western North Pacific, research on wave effects on both TC structure and intensity is limited in this region. In this study, we aim to: (a) show the importance of representation of ocean surface wave related physical processes in a coupled model for TC simulations, and (b) explain how and why these processes affect the TC intensity. For this purpose, this paper is organized as follows: The regional atmosphere-ocean-wave coupled model configuration and five surface wave related physical processes are described in Section 2. Section 3 introduces the data used in this study. The results are presented in Section 4. Finally, the summary and discussion are given in Section 5.

2. Model Description

A regional Atmosphere-Ocean-Wave coupled model has been developed at Fist Institute of Oceanography of Ministry of Natural Resources of China, known as FIO-AOW (Zhao et al., 2017). The framework of FIO-AOW is illustrated in Figure 2. Following an earlier version of the model (Wang et al., 2018; Zhao et al., 2017), the coupler is upgraded from C-Coupler1 to C-Coupler2. A brief introduction to this coupled model and coupling strategy are described in the following subsections.

2.1. Model Components

2.1.1. Atmospheric Model

The Advanced Weather Research and Forecasting model (WRF4.1) (Skamarock et al., 2008) is employed as the atmospheric component of FIO-AOW. WRF is a non-hydrostatic atmospheric model with a wide selection of sub-grid scale parameterizations. It has been widely used in forecasting and studying mesoscale processes including TCs. Following Zhao et al. (2017), the details of model set-up for each component are listed in Table 1. NCEP FNL data is used as the initial and boundary conditions.

2.1.2. Ocean Model

The Princeton Ocean Model (POM) is adopted as the ocean component of FIO-AOW in this paper (Blumberg & Mellor, 1987). POM is a three dimensional model using the Arakawa C grid staggering in the horizontal and terrain-following coordinate in the vertical. The turbulence viscosities and diffusivities are calculated by a 2.5 order Mellor-Yamada turbulence closure scheme (Mellor & Yamada, 1982). In the present study, an optimized and parallelized version of POM (Wang et al., 2010) is employed to represent the dynamical ocean in FIO-AOW. The initial conditions are obtained from the analysis output from an independent ocean-wave coupled forecasting system (POM coupled with MASNUM wave model) which covers the same area as that in this study. The open boundary conditions are provided by the HYCOM reanalysis.

2.1.3. Wave Model

The 3rd generation wave model of MASNUM was developed by Yuan et al. (1991, 1992). The characteristic inlaid method was applied to integrating the wave energy spectrum balance equation. In order to extend the

Table 1
Details of Model Designs

Parameter	WRF	MASNUM	POM
Model domain	0°–50°N, 99°–160°E		
Horizontal resolution	(1/16)°	(1/30)°	(1/30)°
Vertical levels	71	N/A	73
Time step	30 s	60 s	60 s
Coupling frequency	10 min	10 min	10 min
Vertical diffusion scheme	N/A	N/A	Mellor-Yamada
PBL scheme	YSU scheme (Hong et al., 1998)	N/A	N/A
Microphysical scheme	Lin microphysics scheme (Lin et al., 1983)	N/A	N/A
Cumulus scheme	Kain-Fritsch scheme (Kain & Fritsch, 1990)	N/A	N/A
Land surface layer scheme	Noah land surface (Chen & Dudhia, 2001)	N/A	N/A
Shortwave radiation scheme	Duhia shortwave (Dudhia, 1989)	N/A	N/A
Longwave radiation scheme	RRTM longwave (Mlawer et al., 1997)	N/A	N/A
Initial field	NCEP FNL	Hot start	Hot start
Boundary condition	NCEP FNL	JONSWAP	HYCOM reanalysis

model from regional to global scale, the MASNUM wave model in spherical coordinates was developed by Yang et al. (2005). A parallelized version of MASNUM wave model (Wang et al., 2010) is selected as the wave component model in this paper. The spectral discretization for the direction is 36, while the frequency is discretized into 25 bands with a standard increment factor of 1.1 starting from 0.035 Hz. Similar to the initialization of POM, the wave model MASNUM also restarts from the analysis of that forecasting system, while the boundary conditions are taken as JONSWAP spectra (Hasselmann et al., 1980).

2.1.4. Coupler

The C-Coupler2 is used to couple WRF, POM and MASNUM wave model together into the FIO-AOW system. Compared with its earlier version C-Coupler1 (Liu et al., 2014, 2015), C-Coupler2 has a variety of new features, including a common, flexible and user friendly coupling configuration interface; the capability of coupling within one executable or the same subset of MPI (message passing interface) processes; flexible and automatic coupling procedure generation for any subset of component models; dynamic 3D coupling; non-blocking data transfer; and model nesting and adaptive restart capability (Liu et al., 2018), etc.

2.2. Coupling Strategy

In FIO-AOW, The C-Coupler2 is employed as a library to achieve the two-way parallel coupling among the model components. The coupling intervals are set to be 10 min. A new feature of 3D dynamic coupling is used to communicate 3D field between ocean and wave components. It is well known that terrain-following coordinates are widely used in atmosphere and ocean models. In POM, the vertical coordinates are defined as

$$\sigma = \frac{z - \eta}{h + \eta} \tag{1}$$

where z is the depth corresponding to a specified σ layer, η represents the sea surface elevation and h is the sea bottom topography. If sea surface is assumed unperturbed $\eta = 0$, then $z = h \cdot \sigma$, which means z would be a constant. In order to improve computational efficiency, the vertical interpolation weights are usually generated offline and imported before the model integration. Therefore, for a 3D coupling field, it will be interpolated to a fixed depth$z$ at every coupling interval. We refer to this kind of 3D coupling as static 3D coupling (Figure 3a), which is the default way we treat non-breaking surface wave-induced vertical mixing coefficient B_v, which is transferred from MASNUM to POM (Zhao et al., 2017). In fact, the sea surface elevation η is time-varying, which means $z = (h + \eta)\sigma + \eta$ also vary with time. With this latest version of C-Coupler, the vertical interpolation weights are generated online according to the dynamic sea surface. Different from the static 3D coupling, we

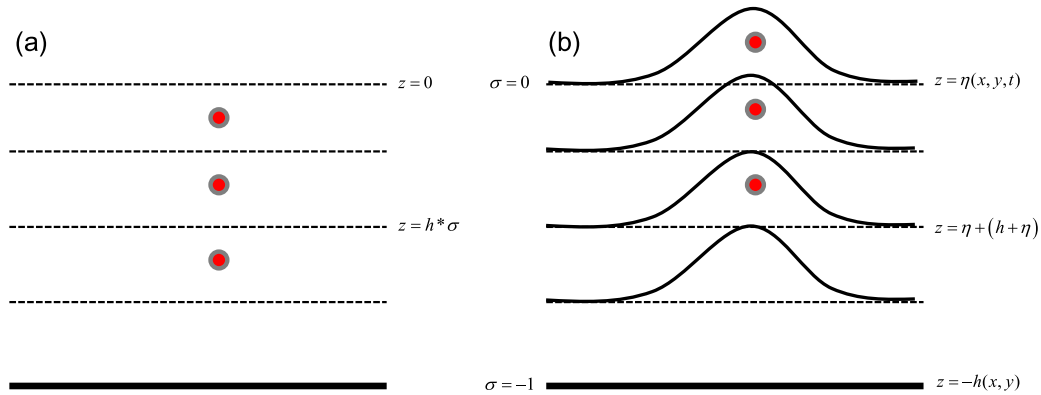

Figure 3. (a) Static 3D coupling, (b) Dynamic 3D coupling.

refer to this kind of 3D coupling as dynamic 3D coupling (Figure 3b). Apparently, the dynamic 3D coupling is much more reasonable and closer to the real ocean. Due to the same model domain and horizontal grid, variables are directly exchanged between the ocean and wave components without interpolation. In contrast, the bilinear interpolation algorithm is used to transform variables between the atmosphere and ocean/wave horizontal grids. To guarantee the consistency and quasi-conservation of flux exchanged between atmosphere and ocean/wave components, the air-sea momentum and enthalpy fluxes are calculated uniformly in atmosphere component by importing necessary variables from ocean and wave components, and then these fluxes are returned to force the ocean and wave models.

Meanwhile, it should be clarified that the "coupling" is not only the connection between two computer programs (models), but also represents the physical interaction between the atmosphere and ocean. From this perspective, the "coupling" involved in this research means to represent the interaction of TC and underlying ocean as realistic as possible. Different from the situation at low to moderate wind conditions, the air-sea interface is no longer a distinct two-layer structure due to the breaking of surface waves under strong winds of TC. Instead, a vapor-liquid mixed layer is formed with the air filling with sea spray droplets and the water filling with bubbles. Within this layer, the wind stress tends to saturated with the increase of wind speed, and the upward enthalpy flux is greatly enhanced by the sea spray. Of note, all these processes could be associated with ocean surface waves. For this reason, the atmosphere, ocean and wave component models in FIO-AOW are physically coupled together through a set of representative ocean surface wave related processes in the literature. Compared to the previous studies (Wang et al., 2018; Zhao et al., 2017), we introduce two additional surface wave related physical processes in the latest version of FIO-AOW which is employed in this paper, one is the wave modulation of air-sea momentum flux, the another is the sea surface current and Stokes drift on air-sea flux. The description of the surface wave related physical processes will be introduced in the following subsections.

2.2.1. Surface Wave Modulation of Air-Sea Momentum Flux

Based on the Monin-Obukhov similarity theory, the wind stress τ_a is parameterized as follows,

$$\tau_a = \rho_a u_*^2 \tag{2}$$

where ρ_a is air density, u_* is friction velocity that is usually tied to the sea surface roughness according to Charnock relation (Charnock, 1955).

$$z_0 = \frac{\alpha_{ch} u_*^2}{g} \tag{3}$$

Here z_0 is sea surface roughness, g is acceleration of gravity, α_{ch} is known as Charnock constant and chosen as 0.0185. Janssen (1989) assumed that the Charnock constant was dependent on wave state. In FIO-AOW, we use the same relationship as ECWMF (Bidlot et al., 2020), and α_{ch} tails off when wind speeds above 33 ms^{-1}. z_0 and α_{ch} have forms of

$$z_o = \frac{\alpha_{ch} u_*^2}{g} + \frac{0.11\nu}{u_*}, \alpha_{ch} = \frac{0.0001 + 0.5(0.0065 - 0.0001)[1 - \tanh(U_{10} - 33)]}{\sqrt{1 - \vec{\tau}_{in}/\vec{\tau}_a}} \quad (4)$$

The wave-induced stress $\vec{\tau}_{in}$ is obtained by integrating the wind-input source function along direction and angular frequency,

$$\vec{\tau}_{in} = \rho_w g \int_0^{2\pi} \int_0^{\infty} \frac{\vec{k}}{\omega} S_{in}(\omega, \theta) d\omega d\theta \quad (5)$$

here ρ_w is seawater density, ω is angular frequency, θ is direction, $\vec{k}$ is wavenumber and $S_{in}(\omega, \theta)$ is wind-input source function.

The wind stress exports momentum flux to surface waves before acts on ocean current. For young surface waves, almost all of momentum flux from atmosphere are absorbed by surface waves. Only after the waves are fully developed, the residual momentum flux will be transferred to ocean. Therefore, the momentum flux at the air-sea interface in FIO-AOW is $\vec{\tau}_a = \vec{\tau}_{oc} + \vec{\tau}_{in} + \vec{\tau}_{diss}$, where

$$\vec{\tau}_{diss} = \rho_w g \int_0^{2\pi} \int_0^{\infty} \frac{\vec{k}}{\omega} S_{diss}(\omega, \theta) d\omega d\theta \quad (6)$$

Here, $\vec{\tau}_{oc}$ is the momentum flux obtained by ocean, and $\vec{\tau}_{diss}$ is momentum flux injected from breaking waves to the ocean, and $S_{diss}(\omega, \theta)$ is wave-dissipation source function. Detailed description of surface waves modulated air-sea momentum flux could be found in Janssen (1989, 1991) and Breivik et al. (2016)

2.2.2. Sea Spray Effect on Air-Sea Enthalpy Flux

The heat and moisture fluxes at air-sea interface could be divided into two parts, the interfacial and the spray modulated fluxes. The interfacial flux is also referred to as turbulent flux, which is dominated by particle irregular fluctuations, while the spray-modulated flux is controlled by the interaction of droplets and their surrounding air. At high wind speeds, the spray-mediated enthalpy flux is comparable to or even larger than the interfacial flux (Andreas, 2010). Thus, the effect of sea spray on air-sea enthalpy flux cannot be ignored, especially for TC simulation and forecasting. Andreas et al. (2008) assumed that the total sensible and latent heat fluxes above the spray evaporation layer are simply linear sums of the spray enthalpy and interfacial fluxes.

$$H_{S,T} = H_S + H_{S,sp} \quad (7)$$

$$H_{L,T} = H_L + H_{L,sp} \quad (8)$$

here H_S and H_L are interfacial sensible and latent heat fluxes, respectively, which could be calculated by the bulk formula as follows

$$H_S = \rho_a c_{pa} u_* t_* \quad (9)$$

$$H_S = \rho_a L_v u_* q_* \quad (10)$$

where c_{pa} is the specific heat of air, u_*, t_* and q_* are Monin-Obukhov related scaling parameters. To facilitate using the sea spray scheme in numerical models, Andreas et al. (2008) proposed a fast sea spray algorithm as follows,

$$H_{S,sp} = \rho_w c_w (T_w - T_{eq,100}) V_S(u_*) \quad (11)$$

$$H_{L,sp} = \rho_w L_v \left\{ 1 - \left[\frac{r(\tau_{f,50})}{50\mu m} \right]^3 \right\} V_L(u_*) \quad (12)$$

where ρ_w is the density of sea water, c_w is the specific heat of sea water, $\tau_{f,50} = \frac{H_{1/3}}{2u_{f,50}}$ is defined as the residence time in the air for the droplets with initial radius of 50 μm, $H_{1/3}$ is significant wave height which can be obtained from surface wave model, $u_{f,50}$ is terminal fall speed of droplets with initial radius of 50 μm. while $r(\tau_{f,50})$

represents the radius of these droplets when they fall back into the sea. L_v is the latent heat of vaporization, T_w is sea surface temperature, $T_{eq,100}$ is defined as the equilibrium temperature of droplets with 100 μm initial radius, $V_s\,(u_*)$ and $V_L\,(u_*)$ are not physical variables, but they are determined based on observational fits (Andreas et al., 2015) and have the forms of

$$V_L(u_*) = \begin{cases} 1.76 \times 10^{-9} & 0 \le u_* \le 0.1358 \\ 2.08 \times 10^{-7} u_*^{2.39} & 0.1358 \le u_* \end{cases}$$
$$V_S(u_*) = \begin{cases} 3.92 \times 10^{-8} & 0 \le u_* \le 0.1480 \\ 5.02 \times 10^{-6} u_*^{2.54} & 0.1480 \le u_* \end{cases} \quad (13)$$

2.2.3. Sea Surface Current and Stokes Drift on Air-Sea Flux

In Equations 2 and 9–13, the friction velocity could be computed by

$$u_*^2 = \left(\frac{\kappa}{\ln\left(\frac{z}{z_0}\right) - \psi_s} \right)^2 S^2 \quad S^2 = U^2 + W_g^2 \quad (14)$$

Here ψ_s is stability function, the horizontal surface wind speed U and convective scaling velocity W_g. Usually, most of models regard the wind speed at lowest model layer as U. Indeed, U represent the mean wind speed relative to the ocean surface (Fairall et al., 1996, 2003). Thus, $U = U_a - U_o$, where U_a is wind speed at a reference height$z$, and U_o is sea surface velocity. Previous studies showed that this ocean current feedback has significant influences on the ocean western boundary current system and atmosphere boundary layer (Renault et al., 2016; Renault & Marchesiello, 2022). In fact, the sea surface velocity could be divided into two parts, the sea surface current velocity and surface wave induced Stokes drift velocity. Recently, the in situ observations by drifters during a hurricane showed that the Stokes drift could account for up to 20% of the sea surface current on average (Curcic et al., 2016). In the light of the bulk formula and in-situ observations (Curcic et al., 2016; Fairall et al., 1996, 2003), both sea surface current and Stokes drift are un-negligible when calculating air-sea flux, which was introduced into climate model for the first time (Bao et al., 2020). Therefore, we calculate U in terms of its original definition in FIO-AOW with the following form

$$U = U_a - U_{oc} - U_s \quad (15)$$

where U_{oc} is sea surface current which could be obtained from the ocean circulation model, while the surface Stokes drift vector can be calculated by integrating the wave spectrum as following

$$\vec{U}_s = \frac{2}{g} \int_0^\infty \int_{-\pi}^{\pi} (\cos\theta, \sin\theta) \omega^3 E(\omega, \theta) d\theta d\omega \quad (16)$$

where $E(\omega, \theta)$ is frequency-direction spectrum.

2.2.4. Rain Induced Ocean Surface Cooling

Heavy rain not only alter the upper ocean stratification, but also has an important impact on air-sea sensible heat flux. It is well known that the raindrops will evaporate and consequently have lower temperature than the sea surface when dropping down from higher altitudes. Generally, the heavier the rainfall, the cooler the sea surface. As a result, the air-sea sensible heat flux under rain conditions is quite different from that under clear sky conditions. In addition, recent theory and in-situ observations suggested that rain could also significantly dampen the short ocean waves and attenuate the swell waves (Cavaleri & Bertotti, 2017; Cavaleri et al., 2015). There is no doubt that the physical mechanisms for rain and marine boundary layer interaction are quite complicated. Understanding of these mechanisms is beyond the scope of this study. Here, a simple hypothesis is made by introducing the rain induced SST cooling (ΔT) to the interfacial sensible heat flux

$$H_S = \rho_a c_{pa} C_T u_* \left[T_a - (T_w - \Delta T)\right] \tag{17}$$

Here, C_T is the Stanton number, and T_a is the surface air temperature. It should be noted that the surface cooling ΔT also depends on wave state, because larger surface waves tend to mix the cool freshwater and thus are not conducive to surface cooling. Details of this hypothesis are referred to Zhao et al. (2017).

2.2.5. Non-Breaking Surface Wave-Induced Vertical Mixing

The mixing induced by non-breaking surface waves that extends to the depth up to wavelength, has been proved to play important role in simulation of the upper-ocean structure (Babanin & Haus, 2009; Dai et al., 2010; Qiao et al., 2004, 2010). The surface waves generated by TCs could accelerate the upper ocean heat losses by the enhancing the vertical mixing (Li et al., 2014; Zhao et al., 2017). In the light of this, the non-breaking wave-induced vertical mixing coefficient B_v proposed by Qiao et al. (2004) is included in FIO-AOW as following:

$$B_v = \alpha \iint E\left(\vec{k}\right) \exp\{2kz\}\, d\vec{k} \frac{\partial}{\partial z} \left(\iint_{\vec{k}} \omega^2 E\left(\vec{k}\right) \exp\{2kz\}\, d\vec{k} \right)^{\frac{1}{2}} \tag{18}$$

where, α is constant and set to 1.0, $E\left(\vec{k}\right)$ is the wavenumber spectrum, and z is depth with $z = 0$ at surface and upward positive. B_v is a three-dimensional variable decreased exponentially with depth, it is usually calculated by wave spectrum model and added to the original viscosity K_{mc} and diffusivity K_{hc} in the ocean circulation model, respectively, in forms of

$$\begin{aligned} K_m &= K_{mc} + B_v \\ K_h &= K_{hc} + B_v \end{aligned} \tag{19}$$

3. Data

3.1. Reanalysis Data Set

The NCEP Final Analysis data (FNL) were output from the Global Data Assimilation System, which assimilated many sources of observation. FNL is available on 1° × 1° grids with 6 h intervals. The FNL data could be accessed via http://rda.ucar.edu/datasets/ds083.2/.

The reanalysis data of the Hybrid Coordinate Ocean Model (HYCOM) (Chassignet et al., 2009) are used to provide boundary conditions for the ocean component in this study. Using the Navy Coupled Ocean Data Assimilation system (Cummings & Smedstad, 2013), satellite SST as well as in-situ vertical profiles of temperature and salinity from XBTs, Argos floats and moored buoys were assimilated. The HYCOM reanalysis is available with a (1/12)°×(1/12)° resolution and 3 h intervals. This reanalysis data was downloaded from this website (http://hycom.org/dataserver/).

3.2. Best-Track Data

To validate the simulated TC track and intensity, 22 TCs (21 TCs in 2013, and 1 TC in 2010) from the best track data provided by the Joint Typhoon Warning Center (JTWC) are adopted as the benchmark. By using Dvorak technique (Dvorak, 1975), all the available observations (buoys, ships and satellites) and numerical weather predictions were analyzed to form best track data set. In addition to TC positions, the 6-hourly maximum sustained 10-m wind speed and minimum sea level pressure are also included. The JTWC data set also provides TC size information including the Radius of maximum wind speed (RMW). The JTWC best-track data is available at https://www.metoc.navy.mil/jtwc.

3.3. Dropsonde Data

The GPS dropsonde data are widely used to study TC boundary layer structure and dynamics (Zhang et al., 2015, 2017, 2018; Zhang & Rogers, 2019). In this paper, A total of 78 dropsonde profiles were collected by

Table 2
Experimental Design

	Fully coupled	Control	Wave coupled
Parameterizations	WRF-POM-MASNUM	WRF-POM	WRF-POM-MASNUM
Wave modulation of momentum flux	Yes	No	Yes
Sea spray effect on air-sea enthalpy flux	Yes	No	No
Sea surface current and Stokes drift on air-sea flux	Yes	No	No
Rain induced ocean surface cooling	Yes	No	No
Non-breaking wave-induced mixing	Yes	No	No

the Hurricane Research Division (HRD) of NOAA during the 5 weather reconnaissance missions into TC Megi on 16 and 17 October 2010. The sampling frequency of dropsonde profiles is 2 Hz, which means the air temperature, pressure, relative humidity, wind speed and direction are recorded every 0.5 s intervals.

3.4. SFMR Data

The surface winds measured by Stepped Frequency Microwave Radiometer (SFMR) were obtained from HRD. As a passive microwave instrument, the data quality of SFMR is reliable when the wind speed stronger than 20 ms^{-1} (Uhlhorn & Black, 2003). The SFMR data was collected from 5 weather reconnaissance missions into TC Megi from 13 to 17 October 2010, and this data is available with 1 s interval.

3.5. AXBT Data

38 profiles of the Airborne EXpendable BathyThermograph (AXBT) data are also collected by HRD. The AXBT could measure ocean temperature as a function of depth. In this paper, the raw profiles were vertically interpolated into 1.5 m intervals from sea surface to 350 m depth.

3.6. Altimeter Data

All the available altimeters retrieved significant wave height data during TC Megi are used in this study, including Jason-1, Jason-2 and Envisat1. These data are provided by the Radar Altimeter Database System (RADS) of the Delft University of Technology (Scharroo et al., 2013).

4. Results

4.1. Experimental Design

To explore the integrated effects of surface wave related physical processes on TC simulation, we design two numerical experiments. One of the two experiments is called Fully coupled experiment, in which WRF, POM and MASNUM wave models are coupled together by the C-Coupler2, and all five wave related physical processes mentioned earlier are considered. The other one is named as Control experiment, in which only WRF and POM are activated, which denotes none of the surface wave related physical processes is introduced. By comparing the Fully coupled experiment with the Control experiment, the ability of the coupled model system to capture the TC, as well as the effects of surface wave related physical processes on TC modeling are evaluated. The experimental settings are summarized in Table 2.

4.2. TCs in 2013

In a case study, we have shown that the surface wave related physical processes play an important role in TC intensity (Zhao et al., 2017). To further study these processes, 21 TCs (Table 3) in 2013 that entering in the model domain (Figure 7b) are investigated by using FIO-AOW. The best track data sets provide TC intensity and size information when a TC vortex is classified as a Tropical Depression (TD) or Tropical Storm (TS). The initial time in the best track data for a given TC is selected as the starting time of a simulation (Table 3).

Table 3
Detail Information of 21 TCs Entering the Model Domain in 2013 in the Western North Pacific

Name	Starting time	Ending time	MSLP (hPa)	Wind (ms^{-1})
YAGI	12:00 UTC 08 Jun	06:00 UTC 12 Jun	982	28.27
LEEPI	00:00 UTC 18 Jun	00:00 UTC 21 Jun	996	17.99
BEBINCA	18:00 UTC 20 Jun	06:00 UTC 24 Jun	996	17.99
RUMBIA	12:00 UTC 28 Jun	12:00 UTC 02 Jul	978	35.98
SOULIK	00:00 UTC 08 Jul	00:00 UTC 14 Jul	929	64.25
JEBI	00:00 UTC 31 Jul	12:00 UTC 03 Aug	978	30.84
UTOR	18:00 UTC 09 Aug	12:00 UTC 15 Aug	926	66.82
TRAMI	00:00 UTC 18 Aug	18:00 UTC 22 Aug	967	38.55
KONG-REY	06:00 UTC 26 Aug	00:00 UTC 30 Aug	985	25.70
TORAJI	18:00 UTC 01 Sep	00:00 UTC 04 Sep	985	25.70
USAGI	18:00 UTC 16 Sep	06:00 UTC 23 Sep	922	69.39
PABUK	06:00 UTC 21 Sep	00:00 UTC 27 Sep	956	46.26
WUTIP	06:00 UTC 27 Sep	00:00 UTC 01 Oct	948	51.44
SEPAT	00:00 UTC 30 Sep	18:00 UTC 02 Oct	993	20.56
FITOW	18:00 UTC 30 Sep	06:00 UTC 07 Oct	956	40.26
DANAS	06:00 UTC 04 Oct	00:00 UTC 09 Oct	933	61.68
NARI	12:00 UTC 09 Oct	18:00 UTC 15 Oct	948	51.44
WIPHA	12:00 UTC 10 Oct	06:00 UTC 16 Oct	933	61.68
FRANCISCO	06:00 UTC 16 Oct	06:00 UTC 26 Oct	918	71.96
KROSA	18:00 UTC 29 Oct	06:00 UTC 04 Dec	944	53.97
HAIYAN	00:00 UTC 04 Dec	06:00 UTC 11 Dec	895	87.38

Note. The TC names are listed in the first column, the starting and ending time of simulation are given in the second and third columns. The last two columns show the lifetime maximum intensity measured as MSLP and maximum wind speed at 10 m from JTWC best track, respectively.

Comparisons of modeled TC track and intensity with the best track are performed. From here on out, the model outputs are post processed using GFDL vortex tracker (Biswas et al., 2018). By using this toolkit, the RMW is derived as well as TC position and intensity. Because the background flow of regional model is mainly constrained by boundary condition, the TC track errors between two experiments have no significant difference. The Mean Absolute Errors (MAE) of TC track are 70.27 and 70.87 km for the Control and Fully coupled experiments, respectively. The scatter plots of intensity biases for all 21 TCs as well as the linear best fits are shown in Figure 4. Similarly to regional coupled model results (Bender & Ginis, 2000) and reanalysis data (Figure 1a), we notice that both the Control and Fully coupled experiments tend to overestimate the intensity of weak TCs but underestimate the strong TCs. However, the intensity underestimation (overestimation), as measured by both Minimum Sea Level Pressure (MSLP) and maximum wind speed at 10m (Figures 4a and 4b), has been mitigated considerably in the Fully coupled experiment. The MAEs are nearly equal at 0 h for the Control and Fully coupled experiments with a value of 3 ms^{-1} (Figure 4c). Since 48h, the effect of surface waves related physical processes becomes to be more pronounced. The MAE in the Control experiment is about 7.57 ms^{-1} at 120 h. In contrast, it reduces to 5.68 ms^{-1} in the Fully coupled experiment at the same lead time. TC intensity errors vary with TC intensity (Figure 4d). In both Fully coupled and Control experiments, the MAEs are quite similar for TD, TS and TC Category 1 (CAT1) TC. However, the surface waves help to reduce the intensity errors in the Fully coupled experiment for Category 2 (CAT2) to Category 5 (CAT5) TCs compared to the Control experiment. For instance, the MAE of CAT5 is 27.89 ms^{-1} in the Control experiment, while it is only 20.78 ms^{-1} in the Fully coupled experiment (Table 4). Furthermore, we compare the modeled wind-pressure relationship with that in the best track. Although both the Control and Fully coupled experiments have weaker maximum wind speed than the best track at a given MSLP in the wind speed range of 35–86 ms^{-1} (Figure 5a), the wind-pressure relationship in the Fully coupled experiment agrees slightly better with the best track data than the Control experiment. Figure 5b shows the histograms of TC intensity from the two experiments compared to best track. It appears that only 18% of the TCs have a strength stronger than 45 ms^{-1} in the Control experiment, which is much smaller than the percentage (27%) in the best track. In contrast, the Fully coupled experiment produces a more realistic distribution (21%) than the Control experiment.

In addition to TC track and intensity, the TC size, as measured by RMW, is also evaluated. It shows that RMW errors also vary with TC intensity (Figure 5c). The surface waves related physical processes help to reduce the RMW error especially for strong storms (CAT2 to CAT5). For instance, the MAE for RMW is 49.02 km for CAT5 in the Control experiment, while it is 39.82 km in the Fully coupled experiment. However, it is found that TDs have the largest RMW errors in the both two experiments. And we also note that the largest MAE occurs at initial time (Figure 5d). In view this, the sum of squares of deviation (SSD) of simulated RMW from the best track at different lead time, is calculated using the following formula

$$SSD = \sum_{i=1}^{i=n} \left(M^i - O^i\right)^2 \tag{20}$$

where M represents the modeled RMW, O denotes the RMW in best track data, and the superscript i represents RMW at a certain lead time. For TD. It follows that the SSD at initial time account for 49% and 52% of the total SSDs in Control and Fully coupled experiments, respectively. The large RMW errors can be attributed to the coarse initial condition which is incapable of resolving small TC scales, and sometimes even fails to resolve a

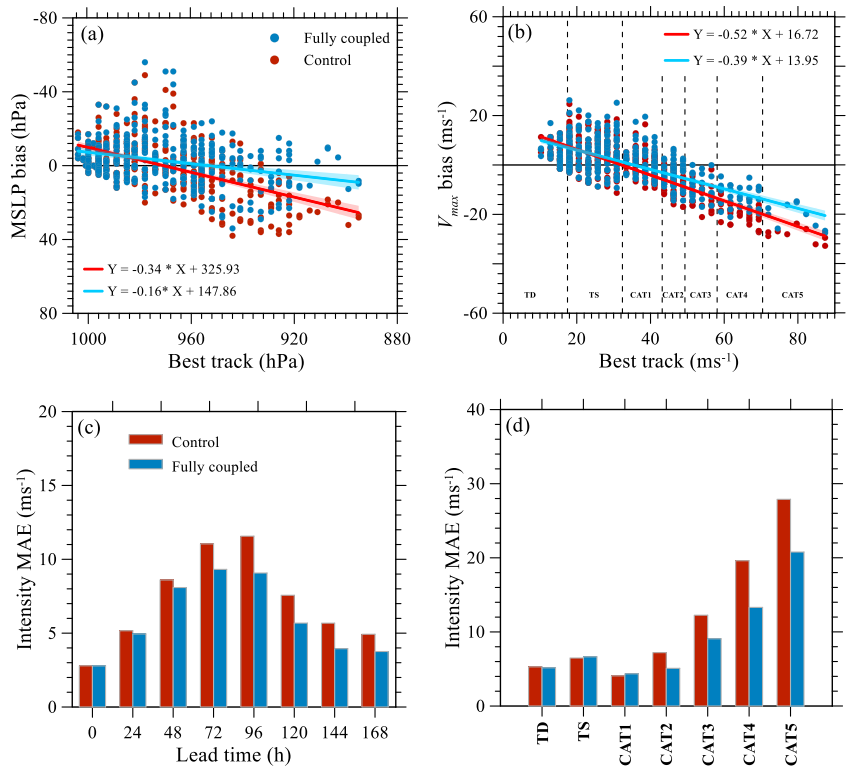

Figure 4. The model biases as measured by (a) MSLP and (b) maximum wind speed at 10m height for all 21 TCs in 2013. (c) MAE of maximum wind speed as function of simulation lead time, (d) MAE of maximum wind speed for different TC categories. The model biases (model minus best track) are calculated 6-hourly during the lifetime of each TC. Linear fits (solid lines) with 95% confidence intervals (shade area) are also shown. In panel (b), by using the dashed lines, the TCs are classified into TD, TS and CAT1 to CAT5 according to the Saffir-Simpson hurricane scale.

TD. Our results confirm that the initial condition is also an important factor for TC size simulations, which is supported by Xu and Wang (2010) and Chan and Chan (2014).

The relationship between the air-sea enthalpy flux and wind speed in the Fully coupled and Control experiments is compared in Figure 6. It appears that air-sea enthalpy fluxes in the two experiments are quite similar for wind speeds below 26 ms^{-1}. However, the enthalpy flux in the Fully coupled experiment increases more rapidly with wind speed than in the Control experiment when the wind speeds exceed 26 ms^{-1}. Due to the sea spray effect, this enthalpy flux enhancement is much more significant within the inner core area than in outer core area (Figure 6). Our result is consistent with Andreas et al. (2015), who documented that sea spray mediated enthalpy flux exceeded the interfacial enthalpy flux at wind speed of about 26 ms^{-1}.

Table 4
Statistics of Intensity for Different TC Categories

		Control		Fully coupled	
Category	Wind (ms^{-1})	MAE (ms^{-1})	ME (ms^{-1})	MAE (ms^{-1})	ME (ms^{-1})
TD	10.79–16.96	5.29	4.96	5.289	4.96
TS	17.47–32.38	6.48	4.79	6.64	4.91
CAT1	32.90–42.15	4.08	−0.19	4.35	1.72
CAT2	42.66–48.83	7.21	−7.11	5.09	−4.14
CAT3	49.34–57.57	12.26	−12.26	9.07	−9.07
CAT4	58.08–69.90	19.61	−19.61	13.31	−13.31
CAT5	≥70.42	27.89	−27.89	20.78	−20.78

4.3. TC Megi

Results from simulations of multiple TCs confirmed the important role of surface wave related physical processes in TC intensity. To explore the underlying mechanisms for the intensity differences between Control and Fully coupled experiments, A case study approach is used. Here, TC Megi in 2010 is selected because of extensive airborne observations. Megi was also the only super typhoon in 2010 in the western North Pacific, JTWC classified it as a tropical depression at 12:00 UTC 13 October. Early on October 17, Megi started to move westward. It reached its lifetime maximum intensity around 18:00 UTC on 17 October and then made its first landfall over Philippines. Therefore, our simulation is integrated from 12:00 UTC 13 to 18:00 UTC 17 October. In order to quantify the effect of wave modulation of

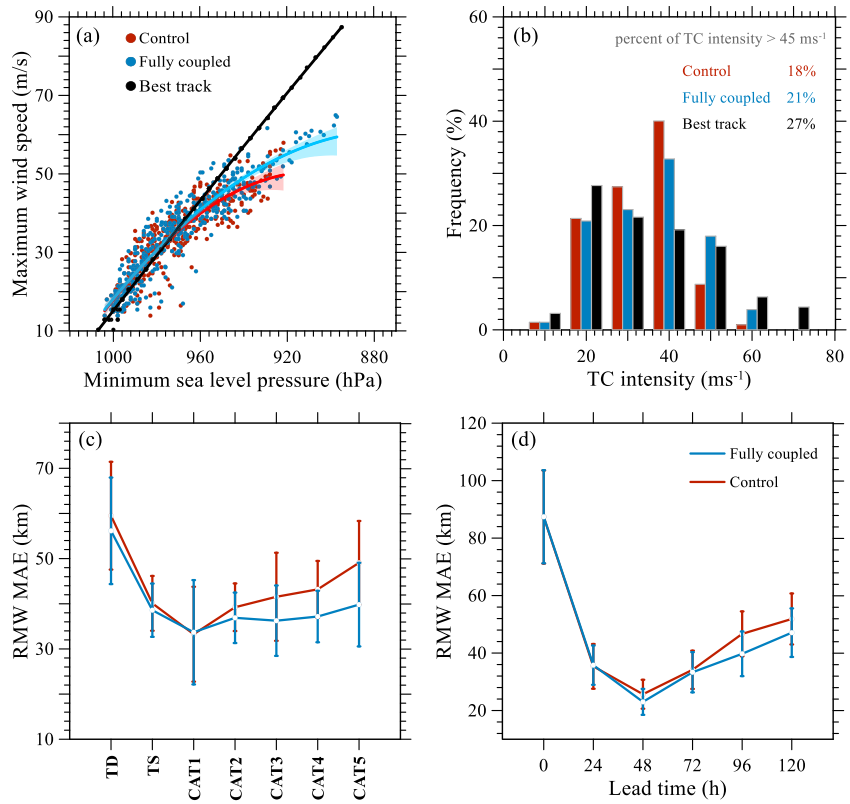

Figure 5. (a) Wind-pressure relationship of Control (red dots) and Fully coupled (blue dots) experiments, compared with the best track (black dots), along with their polynomial fits with 95% confidence intervals (shaded area). (b) Frequency distribution of TC intensity as measured by maximum wind speed, the bin size is 10 ms^{-1}. (c) MAE of RMW for different TC categories, (d) MAE of RMW as function of simulation lead time, the bars in panels (c) and (d) indicate ±2 standard error.

air-sea momentum flux on TC intensity, another experiment called Wave coupled (Table 2) is conducted besides the Control and Fully coupled experiments. The mode set-up of all the three experiment is the same as shown in subsection 4.1.

The simulated tracks of Megi are validated against the JTWC best track. The modeled tracks are generally consistent with the best track until 06:00 UTC16 October (Figure 7c). After that, the modeled tracks move northwestward and deviate from best track. The track differences among the three experiments are almost negligible. TC intensity in the Control and Fully coupled experiments begin to bifurcate at 18:00 UTC 13 October (Figure 7d). While, in the Control and Wave coupled experiments, the bifurcation point occurs at 12:00 UTC 14 October.

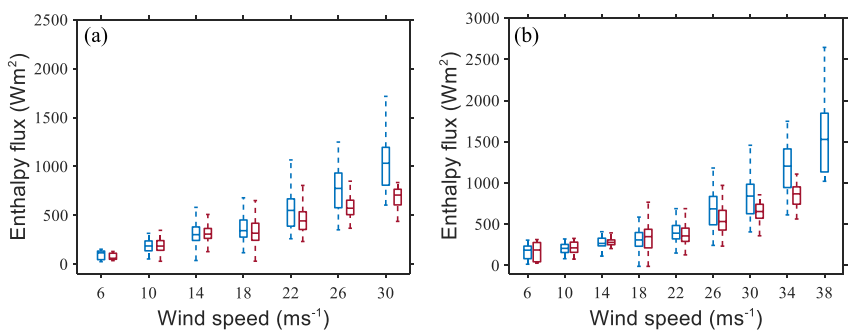

Figure 6. The relationships between air-sea enthalpy flux and 10 m wind speed in Control (red) and Fully coupled (blue) experiments, the air-sea enthalpy flux and 10 m wind speed are averaged within the areas of r/RMW≤5 and r/RMW≤2 in all the simulations, respectively. The upper (lower) whiskers represent maximum (minimum) values, the upper (lower) box bounds represent upper (lower) quartile Q1 (Q3), the box center lines represent median values.

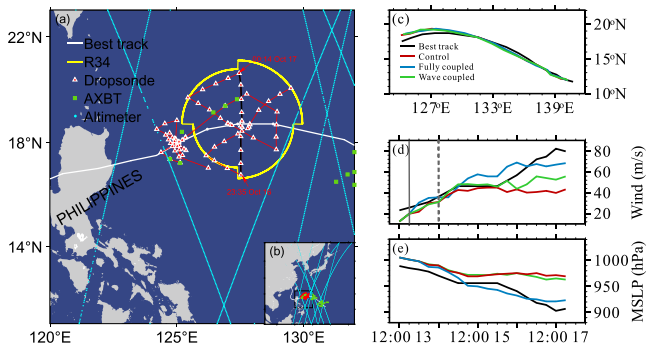

Figure 7. (a) JTWC best track of Megi (white line), AXBT (green squares) and dropsonde (red triangles) deployed positions, the cyan dots represent the available altimeter trajectories closest to TC center during the simulation period, 11 dropsondes along the black line are selected to assess model performance in Figure 9, the estimated 34-knot wind radius (yellow circle) at 00:00 UTC 17 October is also superimposed. (b) Model domain of FIO-AOW. (c) Simulated TC track. (d)Time series of 10 m maximum wind speed, and (e) time series of MSLP. The solid gray line in panel (d) represents intensity divergence point between Control and Fully coupled experiments at 18:00 UTC 13 October. While the dash gray line represents the intensity divergence point between Control and Wave coupled experiments at 12:00 UTC 14 October.

The TCs in the Control and Wave coupled experiment stop deepening until 06:00 UTC 15 October (Figures 7d and 7e). The MAE of intensity is 29 and 28 hPa in in the Control and Wave coupled experiments respectively, while it is reduced to 11 hPa in the Fully coupled experiment. Although there is a about 16 hPa underestimation of intensity at the initial time, our results indicate that the surface wave related physical processes are more conducive to TC intensification and thus lead to better intensity simulation than other experiments.

The modeled ocean vertical temperature profiles are compared with AXBT observations (Figure 8a). The ocean initial conditions of the Control and Fully coupled experiments are both obtained from an operational ocean forecasting system, in which the ocean and wave models are coupled by the non-breaking surface wave-induced vertical mixing. For this reason, the temperature profiles are quite similar between two experiments. As mentioned earlier, sea spray could substantially increase the air-sea enthalpy flux, while wave mixing could enhance the vertical mixing rate in upper-ocean. These two processes together promote the losses of heat in ocean mixed layer, resulting in a larger reduction in upper-ocean temperature. In addition, the shallower mixed layer depth of simulations implies the ocean initialization need to be further improved.

All the available altimeter data closest to TC center is employed. To avoid the influence of TC size discrepancy on verification of significant wave height, the distances of altimeter from TC center are normalized by RMW. Then wave validations are performed near the TC center area ($0<r/RMW\leq10$) and the outer area ($10<r/RMW\leq60$), respectively. As expected, significant wave heights are under estimated in both the Fully coupled and Control experiments (Figures 8b and 8c). Compared to TC outer area, we are more concerned with the model performance near the TC center. Unfortunately, only 1 swath passed through the TC inner core on 14 October. Due to the small difference in TC intensity, the significant wave height in Fully coupled experiment is slightly closer to altimeter observations than that in the Control experiment.

To examine the integrated effect of surface wave related physical processes on the structure of TC Megi, dropsonde observations on board aircraft are analyzed to evaluate the performance of the coupled model. It should be noted that the track errors are not negligible. To facilitate comparison, the dropsondes are relocated in storm-relative framework. The relocation process goes like this: suppose the distance and angle of a dropsonde relative to real TC center are D and β, then shift the dropsonde so that it has the same distance D and angle β relative to the simulated TC center. Then, the model variables such as wind speed and temperature are interpolated into the relocated

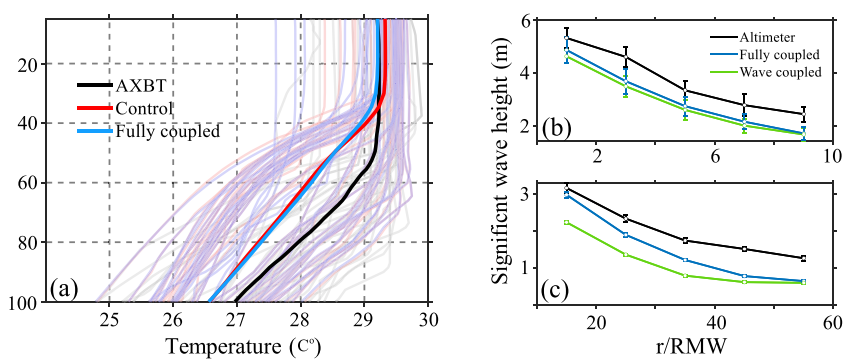

Figure 8. The comparison of observed and modeled (a) vertical ocean temperature, (b) significant wave height within $0<r/RMW\leq10$ area, (c) significant wave height within $10<r/RMW\leq60$ area. In panel (a), the 38 AXBT measured temperature profiles are indicated by gray curves, the red and blue curves are corresponding profiles from Control and Fully coupled experiments, respectively. The bold curves are mean temperature profiles. In panel (b) and (c), the distance of Altimeter trajectories from TC center is normalized by RMW, the bars indicate ±2 standard error in each bin.

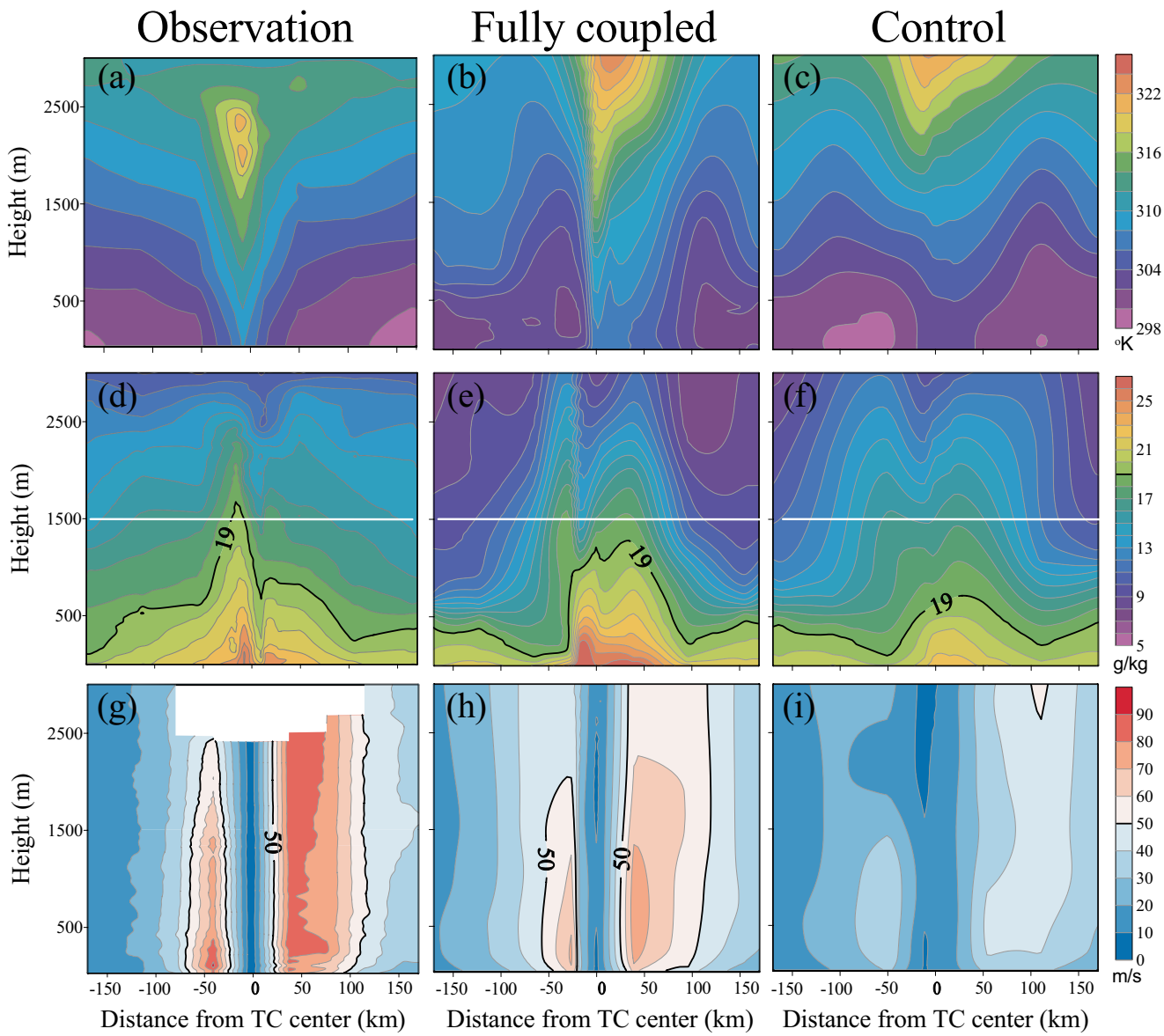

Figure 9. The vertical cross sections of observed (a) potential temperature, (d) water mixing ratio and (g) wind speed along locations of the 11 dropsondes shown in Figure 7a, the time of the first and last of the 11 dropsonde is 23:35 UTC 16 and 00:14 UTC 17 October. Correspondingly, the middle panels (b), (e) and (h) are the same as left panels but for Fully coupled experiment, and the right panels (c), (f) and (i) are for Control experiment. The white lines indicate the 1,500 m height for reference.

positions. It clear that the area of water mixing ratio greater than 19 g/kg in the Fully coupled experiment extents up to 1,300 m, which is in good agreement with that in observation (1,600 m). In contrast, the Control experiment has only a limit area of water mixing ratio reaching 19 g/kg up to about 700 m height (Figures 9d–9f). Despite that the wind speeds in both Control and Fully coupled experiments are weaker than measurement, we notice that the asymmetric structure is better reproduced and wind speeds are relatively stronger in the Fully coupled experiment. In contrast, the Control experiment significantly underestimate the wind speeds in eyewall (Figures 9g–9i).

The azimuthally averaged vertical profiles of simulated wind speeds are compared with observations in the eyewall (defined as region within $0.75 \leq r/RMW \leq 1.25$) and the outer core ($3 \leq r/RMW \leq 5$) regions (Figure 10). In the eyewall region, it is evident that the simulated wind speeds are underestimated in both Control and Fully coupled experiments (Figure 10a). However, the tangential wind speeds in the Fully coupled experiments is much closer to the observations, particularly in the surface layer (Figure 10b). Both two experiments appear a

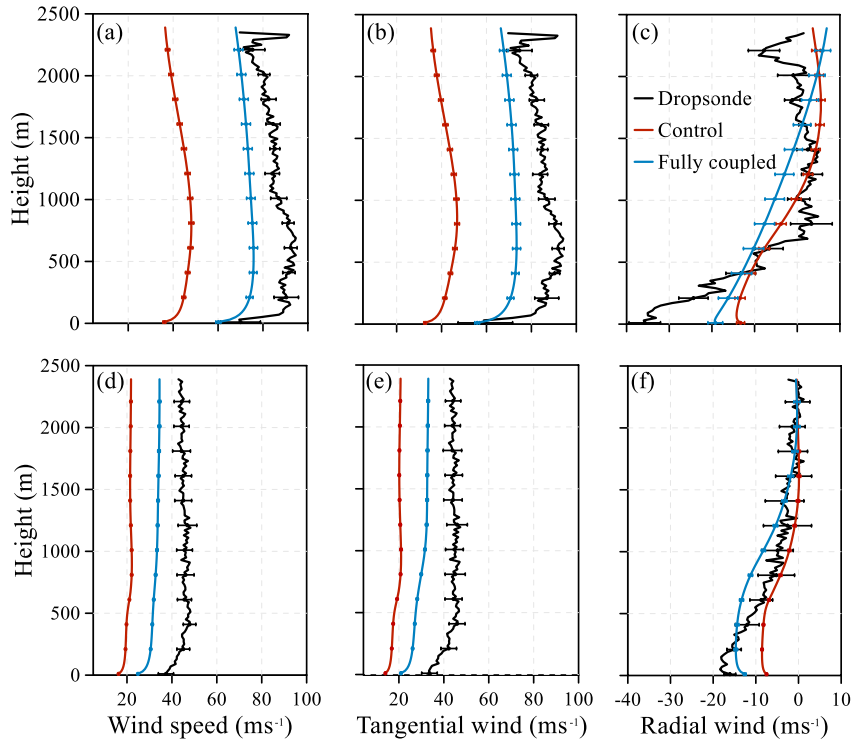

Figure 10. The vertical profiles of (a) wind speed, (b) tangential wind speed and (c) radial wind speed averaged in the eyewall region (0.75≤r/RMW≤1.25) on 17 October. Panels (d), (e) and (f) are the same as (a), (b) and (c), but averaged in the outer core region (3≤r/RMW≤5). The red lines are from Control experiment, the blue lines are from Fully coupled run and the black lines are observed by dropsondes. The bars indicate ±2 standard error in each 20 m height bin, while they are plotted at intervals of 200 m.

weaker peak inflow and deeper boundary layer compared to dropsonde observations (Figure 10c), although the peak inflow in the Fully coupled experiment is closer to the observed value. One possible reason for the deeper inflow layer is the modeled vertical eddy diffusivity is overpredicted (Zhang et al., 2015, 2017, 2018; Zhang & Rogers, 2019). In the outer core region, the tangential wind profile in the Fully coupled experiment agrees better with observations compared to the Control experiment (Figure 10e). Within the TC boundary layer below 500 m, the radial wind profile in the Fully coupled experiment is also closer to observations than in the Control experiment in terms of inflow strength.

The RMW distribution indicates that the modeled TCs are generally characterized by larger RMW compare to SFMR RMW estimates (Figure 11). Only 48% of TCs in the Control experiment have RMWs less than 35 km, a percentage much smaller than that in observations (96%). In contrast, the Fully coupled experiment produces a more realistic RMW distribution with 93% of TCs that have RMWs less than 35 km.

We adopt the same approach to perform model diagnostics as Zhang et al. (2012), the model output is azimuthally averaged and presented as a function of height and radial distance normalized by RMW. The azimuthally mean tangential, radial and vertical wind in the Control and Fully coupled experiments at the intensity bifurcation point are compared in Figure 12. It can be seen that both of the Control and Fully coupled experiments featured with a typical strong outflow located at 10 ~ 16 km altitude, inflow within the 0 ~ 10 km layer, and strong updraft in the eyewall region. However, the axisymmetric vortex is much weaker in the Control experiment than that in the Fully coupled experiment (Figures 12a–12c), the peak inflow, outflow and updraft (Figures 12d–12i) in the Fully coupled experiment are stronger than those in the Control experiment, even though the TC intensity, as measured by maximum wind speed at 10 m, is essentially the same in the two experiments at the intensity bifurcation point (Figure 7d).

The equivalent potential temperature θ_e inside the eyewall is larger in the Fully coupled experiment than that in the Control experiment (Figures 13a–13c). The thermodynamic mixed layers in the two experiments are generally

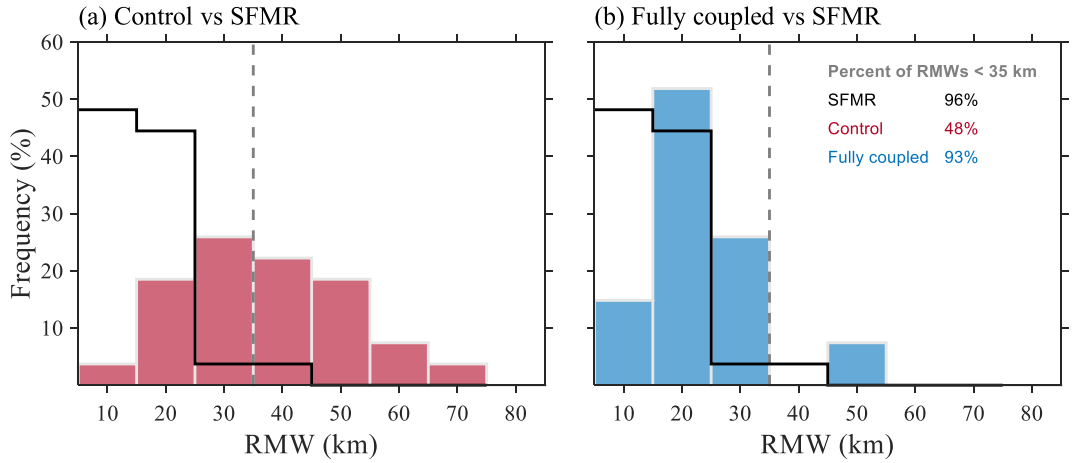

Figure 11. Frequency distribution of surface RMW at 10 m height in (a) Control and (b) Fully coupled experiments. The black lines in panels (a) and (b) show the frequency distribution of RMW observed by SFMR for reference, the percentages of RMWs within 35 km threshold (dashed gray lines) for simulations and observations are shown in panel (b).

similar, with the mixed layer being slightly shallower in region of 1≤r/RMW≤2 in the Control experiment. There is a more unstable layer in Fully coupled experiment below 200 m ((Figures 13d–13f). A warmer boundary layer with a more unstable surface layer in the Fully coupled experiment, favors the convection development and thus enhances the secondary circulation. This could be mainly attributed to the air-sea vapor and enthalpy fluxes are substantially enhanced in the Fully coupled experiment (Figures 14a–14e). Given that the azimuthally mean surface wind stresses are approximately the same between the Control and Fully coupled experiments (Figure 14f), sea spray effect plays an important role in TC intensification, which is consistent with Zhao et al. (2017).

Next, we evaluate the surface wave effects on TC intensification dynamics. The absolute angular momentum (M) of an air particle is defined as

$$M = rV_t + \frac{1}{2}fr^2 \tag{21}$$

where r represents the distance from TC center, V_t is tangential wind speed and f is Coriolis parameter. Equation 21 can be also written as $V_t = \frac{M}{r} - \frac{1}{2}fr$, obviously the tangential wind V_t would increase (decrease) with the increase (decrease) of M at a certain r. To diagnose the dynamical mechanism that might cause the intensity change, budget analyses of absolute angular momentum are performed. Follow Zhang and Marks (2015), the budget equation is given by

$$\frac{\partial\langle M\rangle}{\partial t} = -\langle V_r\rangle\frac{\partial\langle M\rangle}{\partial r} - \langle w\rangle\frac{\partial\langle M\rangle}{\partial z} - \left\langle V_r'\frac{\partial M'}{\partial r}\right\rangle - \left\langle w'\frac{\partial M'}{\partial z}\right\rangle + F_r \tag{22}$$

Where V_r represents radial wind speed, w is vertical wind speed. The brackets denote an azimuthal average at a certain height, and the primes represent a departure from the azimuthal mean. In Equation 22, the left-hand term $\frac{\partial\langle M\rangle}{\partial t}$ represents time tendency of azimuthally averaged absolute angular momentum, the right-hand terms are the mean radial advection term $-\langle V_r\rangle\frac{\partial\langle M\rangle}{\partial r}$, the mean vertical advection term $-\langle w\rangle\frac{\partial\langle M\rangle}{\partial z}$, the mean radial eddy transport term $-\left\langle V_r'\frac{\partial M'}{\partial r}\right\rangle$, the mean vertical eddy transport term $-\left\langle w'\frac{\partial M'}{\partial z}\right\rangle$, and the residual term F_r that contributed by subgrid turbulent processes. The time tendency term $\frac{\partial\langle M\rangle}{\partial t}$, the total mean advection term $-\langle V_r\rangle\frac{\partial\langle M\rangle}{\partial r} - \langle w\rangle\frac{\partial\langle M\rangle}{\partial z}$, the total eddy transport term $-\left\langle V_r'\frac{\partial M'}{\partial r}\right\rangle - \left\langle w'\frac{\partial M'}{\partial z}\right\rangle$ and the residual term F_r at the time when TC intensity starts to bifurcate in Fully and Control experiments (Figure 7d) are shown in Figure 15. Not only in the eyewall region, but also within the lowest 500 m in the boundary layer, the time tendency term is larger in Fully coupled experiment than that in the Control experiment (Figure 15c). Relative to the total eddy transport term, the total mean and residual terms make the largest contributions to the gain and loss of time tendency term

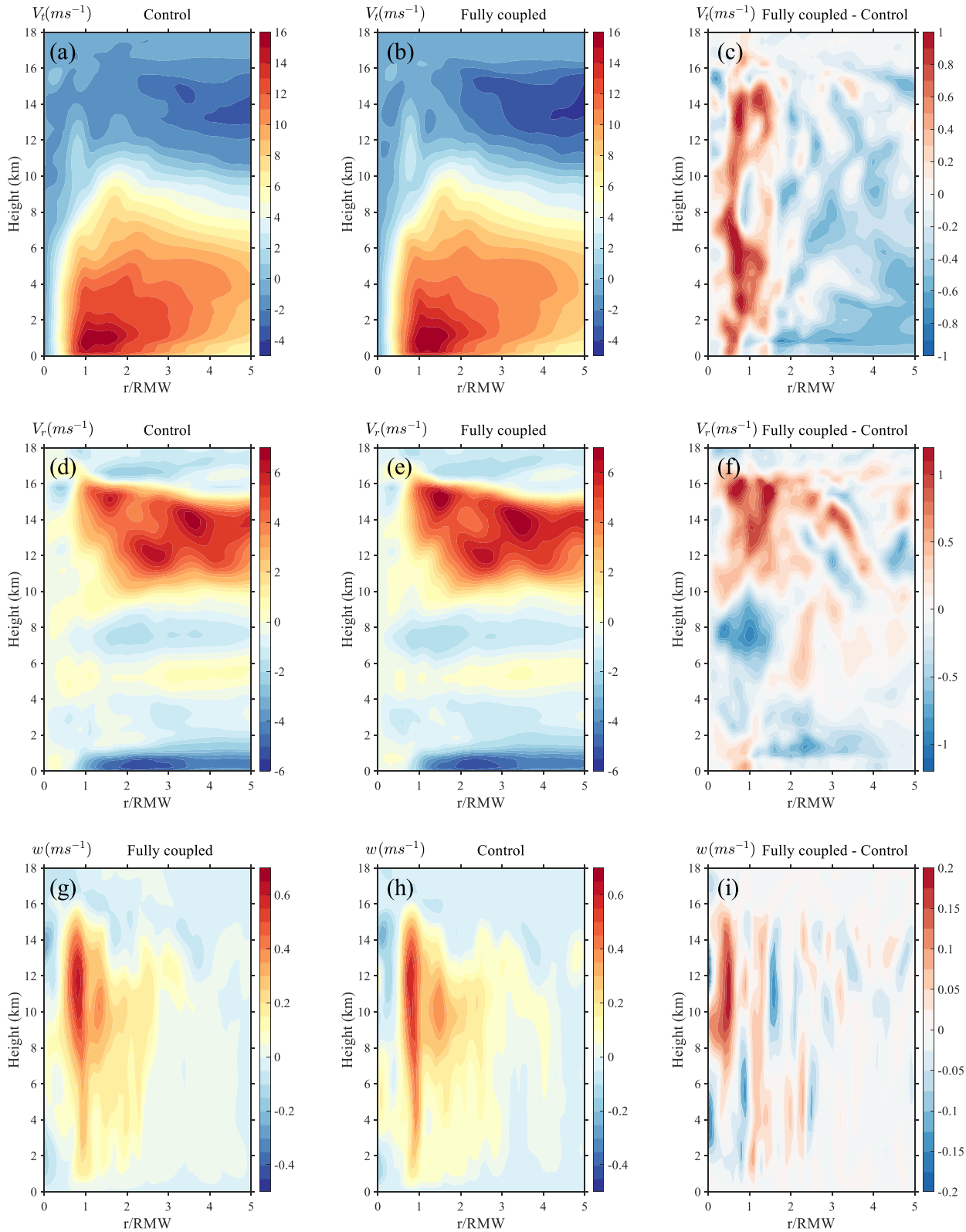

Figure 12. The azimuthally averaged (a) tangential, (d) radial and (g) vertical wind speed as a function of r/RMW and height in Control experiment at 18:00 UTC 13 October. The middle panels (b), (e) and (h) are the same as the left panels but for Fully coupled experiment. The right panels (c), (f) and (i) are the differences between Fully coupled and Control experiments.

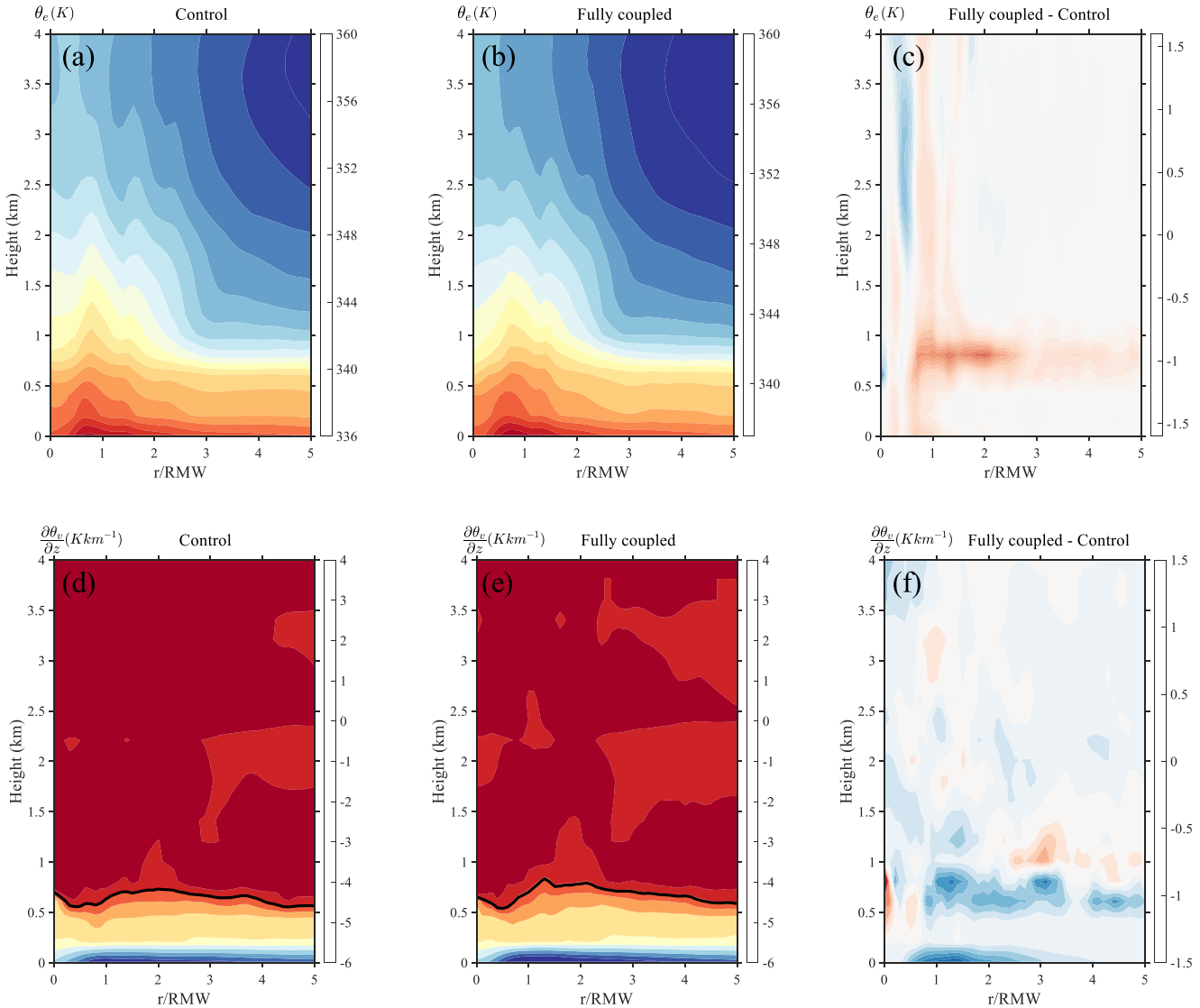

Figure 13. The azimuthally averaged (a) equivalent potential temperature and (d) the vertical gradient of virtual potential temperature as a function of r/RMW and height in Control experiment at 18:00 UTC 13 October. The middle panels (b) and (e) are the same as left panels but for Fully coupled experiment. The right panels (c) and (f) are the differences between Fully coupled and Control experiments. The black curves in panels (d) and (e) represent the depth of thermodynamic mixed layer.

in the boundary layer (Figures 15d, 15e, 15j, and 15k). However, due to the stronger inflow in boundary layer and deeper vertical convection in mid-to upper atmosphere around eyewall region (Figure 12), the total mean advection term is larger in the Fully coupled experiment compared to the Control experiment (Figure 15f). Consequently, the larger total mean advection term helps spinup the vortex faster and lead to stronger tangential wind in the Fully coupled experiment (Figure 12). Although the magnitude is small, the negative total eddy transport term together with residual term offset the positive total mean advection term in low-level atmosphere. Around the eyewall region in mid-to upper-level atmosphere, the negative total eddy transport term cancels the positive total mean advection term by itself. In boundary layer, the mean advection dominates the sum of the eddy advection and frictional effect. The spin-up of the tangential circulation in the boundary layer is associated with the radial inflow generated by agradient force (Montgomery & Smith, 2014; Smith et al., 2009), which is defined as the difference between pressure gradient force and the sum of centrifugal and Coriolis forces in the form of

$$AF = -\frac{1}{\rho}\frac{\partial p}{\partial r} + \frac{V_t^2}{r} + fV_t \tag{23}$$

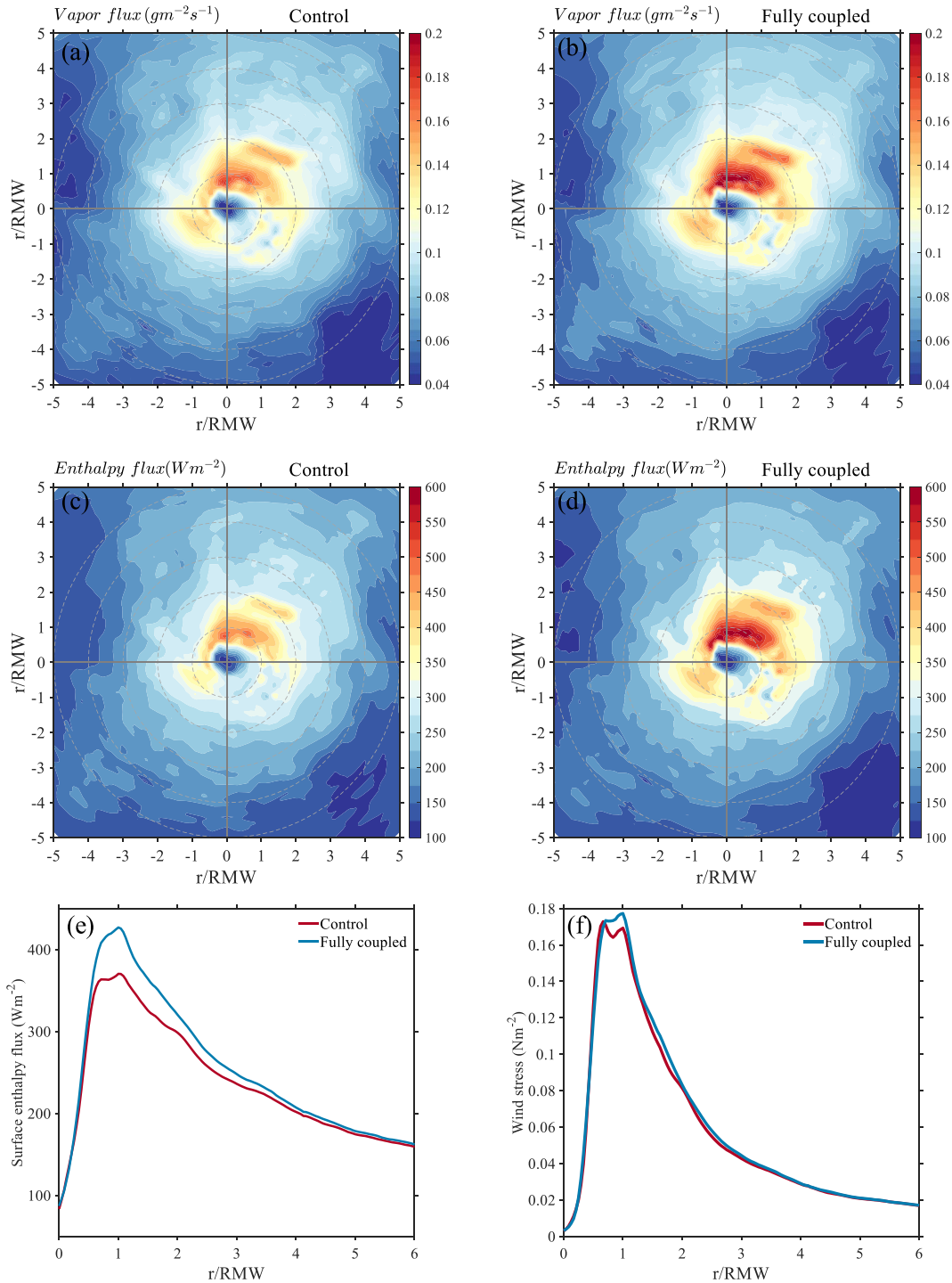

Figure 14. The horizonal view of surface (a) vapor flux and (c) enthalpy flux in Control experiment at 18:00 UTC 13 October. Panels (b) and (d) are the same as left panels but for Fully coupled experiment. (e) The azimuthally averaged surface enthalpy flux. (f) The azimuthally averaged surface wind stress. The 1 ~ 5 times RMW are marked with gray dashed circles.

where P is air pressure and ρ is air density, when $AF > 0$, the tangential wind is supergradient. Figure 16 shows the maximum azimuthally averaged agradient force, which is positive in both two experiments. However, it is larger in the Fully coupled experiment for almost all lead times except the period from 18:00 UTC 14 to 00:00 UTC 15 October, corresponding to weaker TC intensity during the same period (Figure 7d). The larger agradient force in the Fully coupled experiment tend to produce a stronger radial inflow in the boundary layer, which will

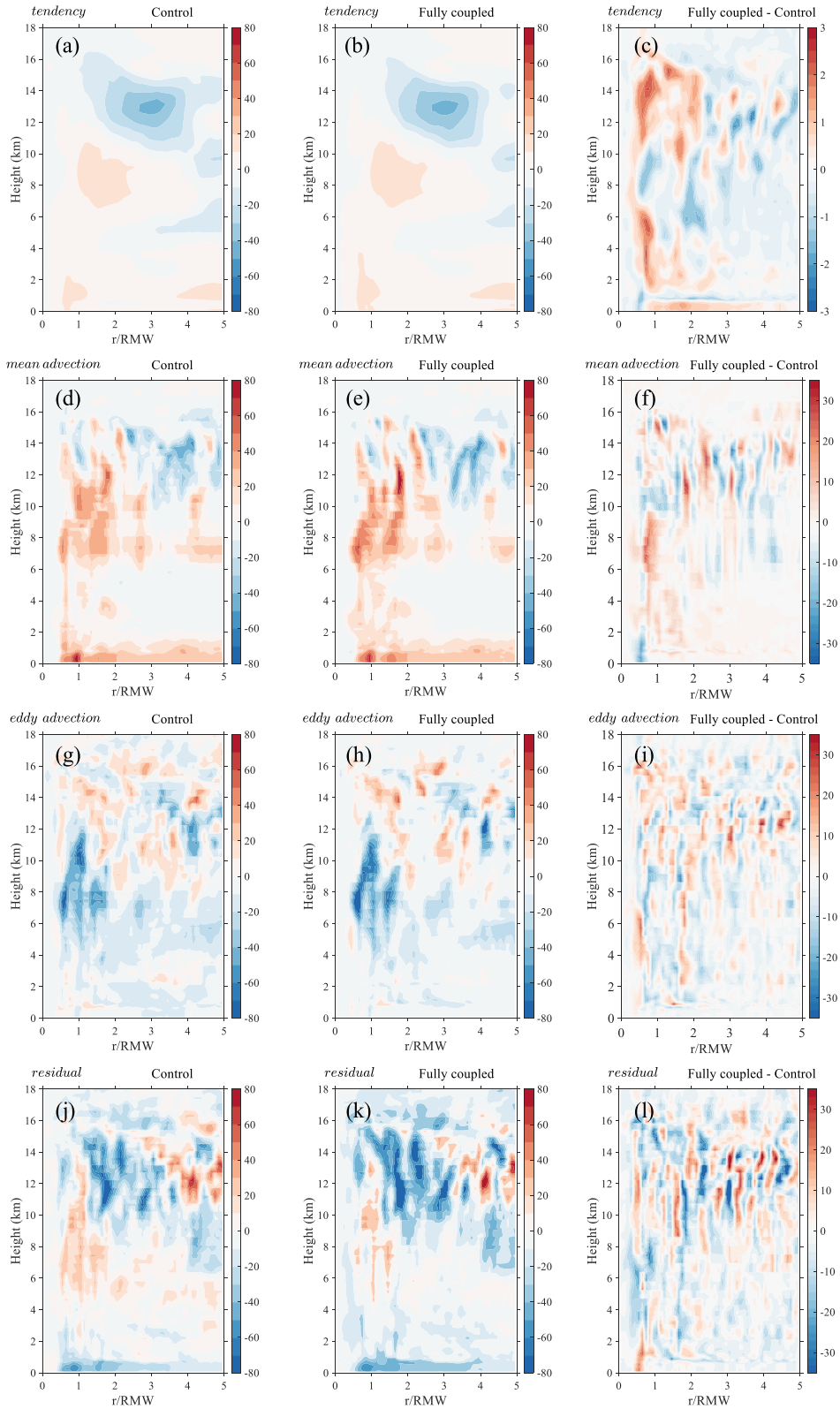

Figure 15. The radius-height plots of the terms in azimuthally averaged absolute angular momentum budget (a) time tendency term, (d) total mean advection term, (g) total eddy transport term and (j) residual term in Control experiment at 18:00 UTC 13 October. The middle panels (b), (e), (h) and (k) are the same as the left panels but for Fully coupled experiment. The right panels (c), (f), (i) and (l) are the differences between Fully coupled and Control experiments.

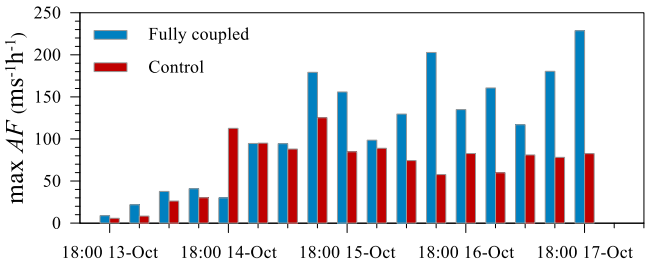

Figure 16. Times series of maximum azimuthally averaged agradient force per unit mass.

bring more inward advection of absolute angular momentum to spinup the tangential winds, leading to a more quickly intensified TC. The results are consistent with the intensification theory of Smith et al. (2009).

To isolate the contribution of wave modulation of air-sea momentum flux to TC intensity, a comparison of azimuthally averaged wind between Control and Wave coupled experiments at the intensity bifurcation point (Figure 7d) is shown in Figure 17. Although having the same TC intensity, the tangential winds and the updraft of Wave coupled experiment in the eyewall region are stronger than those of Control experiment. In addition, the equivalent potential temperature θ_e and water mixing ratio inside the eye and eyewall are higher in the Wave coupled experiment compared to the Control experiment (Figure 18). Outside the eyewall, the boundary layer is more unstable in the Wave coupled experiment. The warmer and moister unstable boundary layer is associated with the enhanced air-sea enthalpy flux (Figures 19a–19c). There is also an increase in surface wind stress in the Wave coupled experiment (Figures 19d–19f). The budget analysis of absolute angular momentum indicates the contribution of total eddy transport term is almost comparable with the total mean advection term in boundary layer (not shown). However, the total mean and eddy advection terms in the Wave coupled experiment are larger than that in the Control experiment, resulting in stronger tangential wind in the Wave coupled experiment. Our results thus suggest that the surface waves act as positive feedback on TC intensification through regulating the exchange of air-sea momentum flux.

5. Summary and Discussion

Although numerous studies emphasize that ocean surface waves play important role in TC intensity simulations. However, most of them are limited to individual TC case study. In this paper, twin numerical experiments, a Control and Fully coupled runs are performed using a regional atmosphere-ocean-wave coupled model. Five representative ocean surface wave related processes are considered in the Fully coupled simulation, including the wave modulation of air-sea momentum flux, sea spray induced air-sea enthalpy flux, sea surface current and Stokes drift on air-sea flux, non-breaking wave-induced vertical mixing on upper-ocean and rainfall induced sea surface cooling. For the first time, TCs of a whole year in western North Pacific are retrospectively simulated to investigate the effects of ocean surface waves on TC intensity. Results suggest that the surface wave related physical processes have a limited impact on track but play an important role in TC intensity and size simulations. The intensity and size (RMW) errors are significantly reduced in the Fully coupled experiment for strong TCs (CAT2 to CAT5) after 48 h. In contrast, their effects on TD, TS and CAT1 TCs are relatively small.

TC Megi in 2010 is chosen as a case study due to available airborne observations in western North Pacific. Results show that TC intensity, structure and size in the Fully coupled simulation agree better with observations compared to the Control simulation. Surface waves tend to increase air-sea momentum flux, which induces strong inflow near the eyewall. The surface wave related physical processes including sea spray effect enhance the air-sea enthalpy fluxes, resulting in a warmer boundary layer and more unstable surface layer that favor convection development. The stronger updraft advects more absolute angular momentum vertically, in favor of spinning up tangential wind above the boundary layer. Within the boundary layer, the larger agradient force can be archived and thereby leads to stronger radial inflow, which tends to advect more absolute angular momentum toward to the eyewall in the Fully coupled experiment. Ultimately, an increase in the absolute angular momentum leads to a faster spin-up of the tangential winds in the inner core region, which is consistent with the boundary layer spin-up mechanism of Smith et al. (2009). Compared to dropsonde and SFMR observations, the introduction of surface wave related physical processes leads to improved TC structure in terms of boundary layer height, inflow strength, and TC size.

Our results emphasize the importance of accurate representation of surface wave related physical processes in TC simulation, in agreement with previous studies (Bao et al., 2011; Garg et al., 2018; Liu, Liu, et al., 2011; Perrie et al., 2005; Xie et al., 2010; Zweers et al., 2015). As documented in the literature, breaking wave induced sea spray could significantly enhance the air-sea heat flux, which acts as positive feedback on TC intensity. On the other hand, the non-breaking wave-induced vertical mixing and rainfall induced sea surface cooling increase

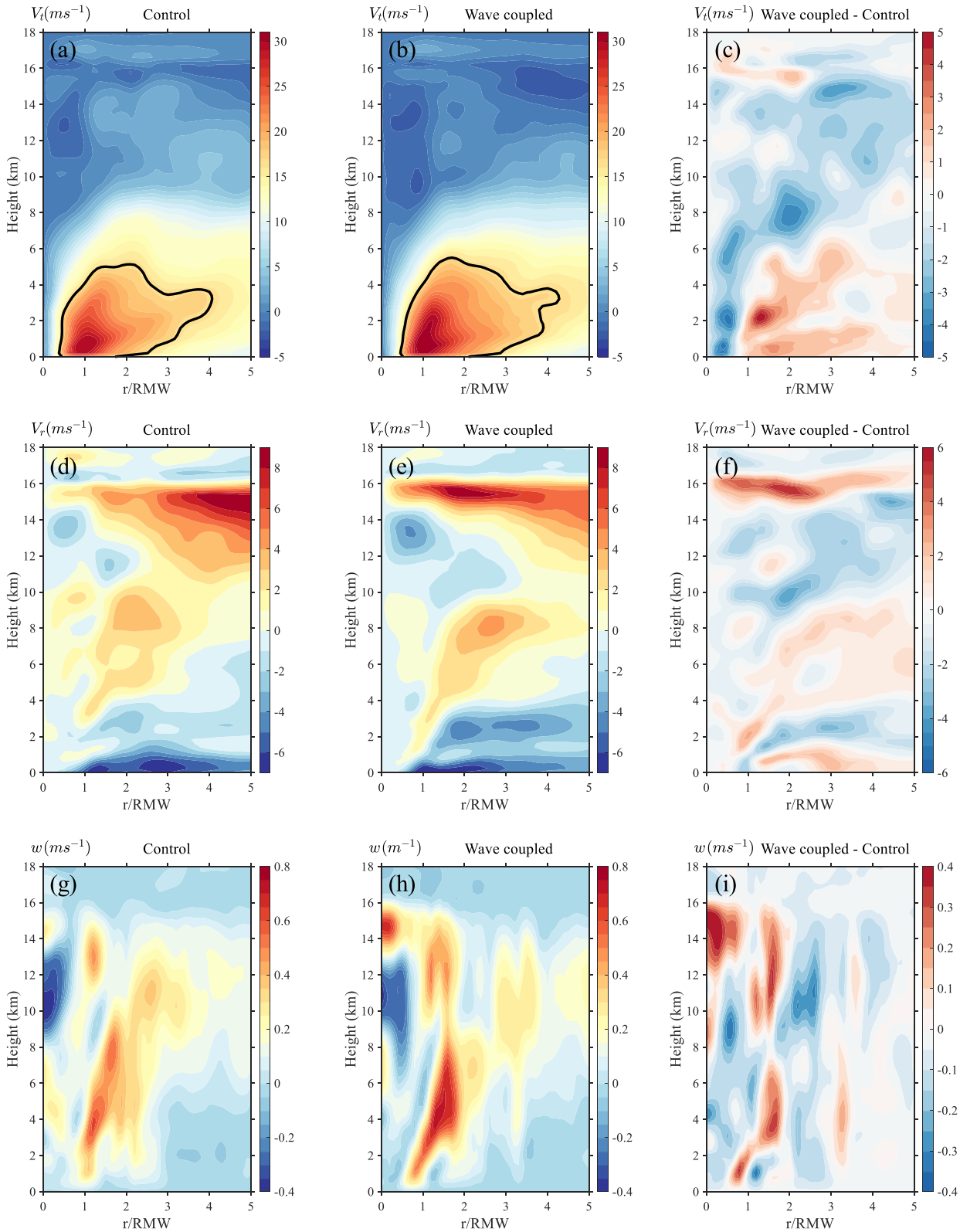

Figure 17. The azimuthally averaged (a) tangential, (d) radial and (g) vertical wind speed as a function of r/RMW and height in Control experiment at 12:00 UTC 14 October. The middle panels (b), (e) and (h) are the same as the left panels but for Wave coupled experiment. The right panels (c), (f) and (i) are the differences between Wave coupled and Control experiments. The black curves in panels (a) and (b) represent 17 ms^{-1} isotach.

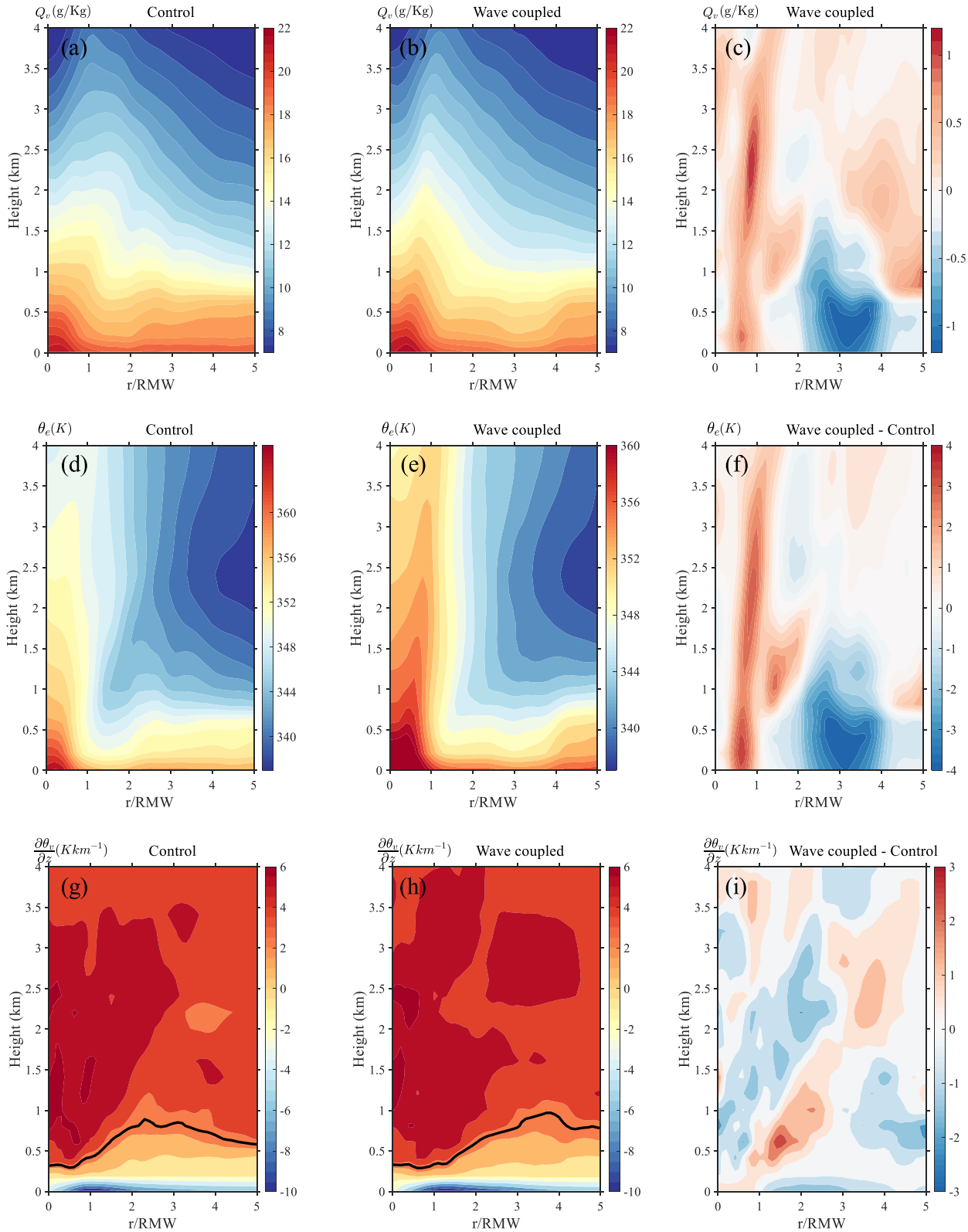

Figure 18. The azimuthally averaged (a) water mixing ratio, (d) equivalent potential temperature and (g) the vertical gradient of virtual potential temperature as a function of r/RMW and height in Control experiment at 12:00 UTC 14 October. The middle panels (b), (e) and (h) are the same as left panels but for Wave coupled experiment. The right panels (c), (f) and (i) are the differences between Wave coupled and Control experiments. The black lines in panels (g) and (h) represent the depth of thermodynamic mixed layer.

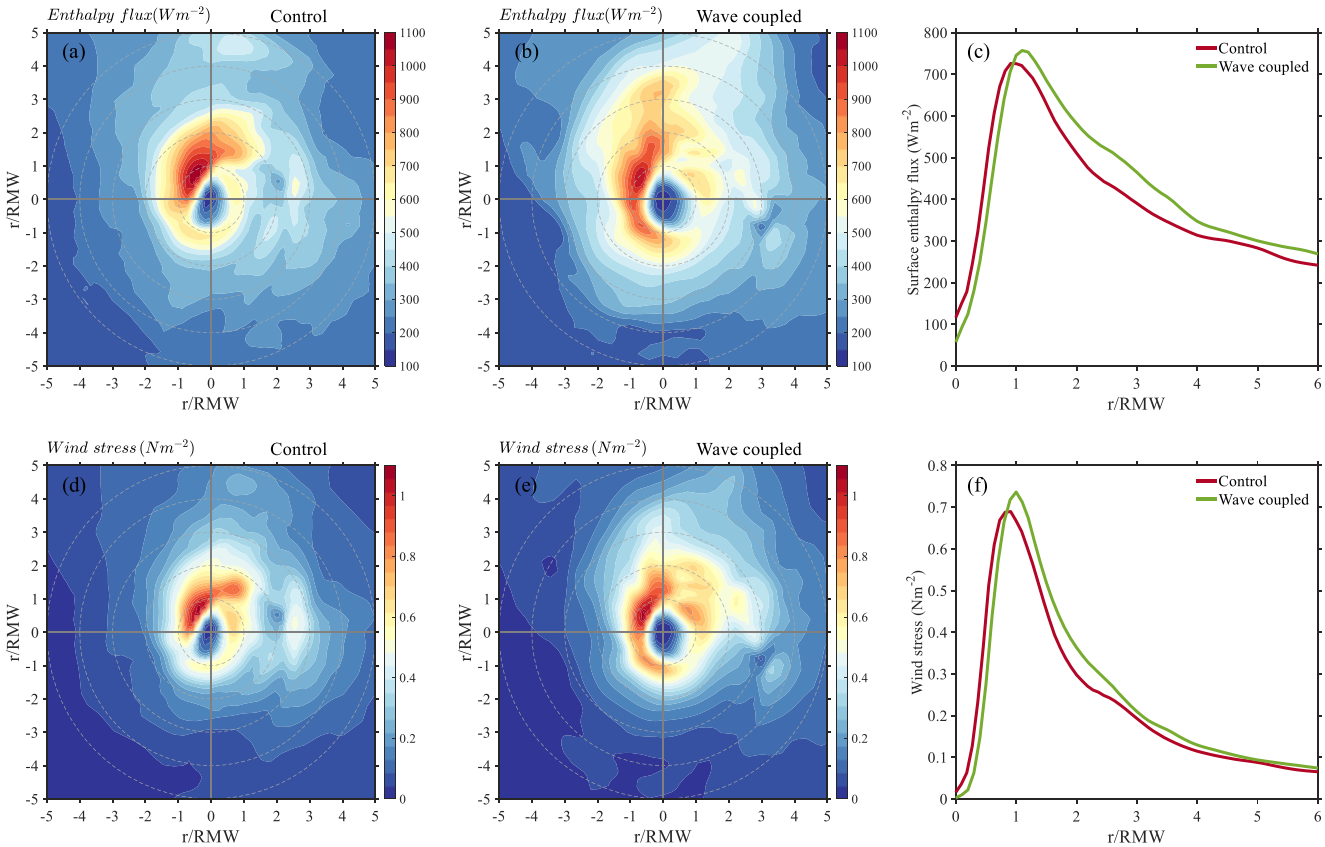

Figure 19. The horizonal view of (a) surface enthalpy flux and (d) surface wind stress as a function of r/RMW and height in Control experiment at 12:00 UTC 14 October, (b) and (e) are the same as (a) and (d) but for Wave coupled experiment. (c) The azimuthally averaged enthalpy flux. (f) The azimuthally averaged surface wind stress. The 1 ~ 5 times RMW are marked with gray dashed circles.

ocean's negative feedback on TC intensity. Indeed, all these processes work concurrently, the negative and positive feedbacks of surface waves processes compete against each other, and each of them could be dominant under certain condition. Our results suggest that the integrated effects of these wave related physical processes positively contribute to storm intensification especially for strong storms. In addition to aforementioned five surface wave related physical processes, other surface wave related physical processes such as wave state dependent sea salt aerosol, sea surface albedo and attenuation of surface waves by rainfall (Cavaleri & Bertotti, 2017), may also have an important impact on TC simulation and should be considered in future studies.

Acknowledgments

This work was mainly supported by the National Key Research and Development Program of China (2016YFA0602204 and 2017YFC1404004) and the National Natural Science Foundation of China (41821004, 41976201, 41506038 and 41875057). Jun Zhang acknowledges support from the U.S. Office of Naval Research Grant N00014-20-1-2071, and National Oceanic and Atmospheric Administration Grants NA21OAR4590370, NA220OAR4590174, and NA22OAR4590178. This paper is a contribution to both the UN Decade Collaborative Centre on Ocean-Climate Nexus and Coordination Amongst Decade Implementing Partners in P. R. China (DCC-OCC) and A Predicted Ocean of UN Ocean Decade.

Data Availability Statement

The model data used in this manuscript can be accessed from https://doi.org/10.5281/zenodo.6682397. The ERA5 data used in this study were downloaded from https://cds.climate.copernicus.eu. The FNL data were obtained from https://rda.ucar.edu/datasets/ds083.2/. For XseaFlux data, people can contact Dr Jiping Liu for permission. Access to other public datasets in this study is described in Section 3.

References

Andreas, E. L. (2010). Spray-mediated enthalpy flux to the atmosphere and salt flux to the ocean in high winds. *Journal of Physical Oceanography*, *40*(3), 608–619. https://doi.org/10.1175/2009jpo4232.1

Andreas, E. L., & Emanuel, K. A. (2001). Effects of sea spray on tropical cyclone intensity. *Journal of the Atmospheric Sciences*, *58*(24), 3741–3751. https://doi.org/10.1175/1520-0469(2001)058<3741:eossot>2.0.co;2

Andreas, E. L., Mahrt, L., & Vickers, D. (2015). An improved bulk air-sea surface flux algorithm, including spray-mediated transfer. *Quarterly Journal of the Royal Meteorological Society*, *141*(687), 642–654. https://doi.org/10.1002/qj.2424

Andreas, E. L., Persson, P. O. G., & Hare, J. E. (2008). A bulk turbulent air-sea flux algorithm for high-wind, spray conditions. *Journal of Physical Oceanography*, *38*(7), 1581–1596. https://doi.org/10.1175/2007jpo3813.1

Babanin, A. V., & Haus, B. K. (2009). On the existence of water turbulence induced by nonbreaking surface waves. *Journal of Physical Oceanography*, *39*(10), 2675–2679. https://doi.org/10.1175/2009jpo4202.1

Bao, J.-W., Fairall, C. W., Michelson, S. A., & Bianco, L. (2011). Parameterizations of sea-spray impact on the air–sea momentum and heat fluxes. *Monthly Weather Review*, *139*(12), 3781–3797. https://doi.org/10.1175/mwr-d-11-00007.1

Bao, Y., Song, Z., & Qiao, F. (2020). FIO-ESM Version 2.0: Model description and evaluation. *Journal of Geophysical Research: Oceans*, *125*(6). https://doi.org/10.1029/2019jc016036

Bender, M. A., & Ginis, I. (2000). Real-case simulations of hurricane-ocean interaction using a high-resolution coupled model: Effects on hurricane intensity. *Monthly Weather Review*, *128*(4), 917–946. https://doi.org/10.1175/1520-0493(2000)128<0917:rcsoho>2.0.co;2

Bernardet, L., Tallapragada, V., Bao, S., Trahan, S., Kwon, Y., Liu, Q., et al. (2015). Community support and transition of research to operations for the hurricane weather research and forecasting model. *Bulletin of the American Meteorological Society*, *96*(6), 953–960. https://doi.org/10.1175/bams-d-13-00093.1

Bidlot, J.-R., Prates, F., Ribas, R., Mueller-Quintino, A., Crepulja, M., & Vitart, F. (2020). Enhancing tropical cyclone wind forecasts (ECMWF Newsletter No. 164). Retrieved from https://www.ecmwf.int/node/19721

Biswas, M. K., Stark, D., & Carson, L. (2018). GFDL Vortex Tracker Users' Guide V3.9a.

Blumberg, A. F., & Mellor, G. L. (1987). A description of a three-dimensional coastal ocean circulation model. In N. S. Heaps (Ed.), *Three-Dimensional Coastal Ocean Models* (pp. 1–16). AGU. https://doi.org/10.1029/co004p0001

Breivik, Ø., Bidlot, J.-R., & Janssen, P. A. E. M. (2016). A Stokes drift approximation based on the Phillips spectrum. *Ocean Modelling*, *100*, 49–56. https://doi.org/10.1016/j.ocemod.2016.01.005

Bruneau, N., Toumi, R., & Wang, S. (2018). Impact of wave whitecapping on land falling tropical cyclones. *Scientific Reports*, *8*(1), 652. https://doi.org/10.1038/s41598-017-19012-3

Cavaleri, L., & Bertotti, L. (2017). The attenuation of swell waves by rain. *Geophysical Research Letters*, *44*(20), 10504–10510. https://doi.org/10.1002/2017gl075458

Cavaleri, L., Bertotti, L., & Bidlot, J.-R. (2015). Waving in the rain. *Journal of Geophysical Research: Oceans*, *120*(5), 3248–3260. https://doi.org/10.1002/2014jc010348

Chan, K. T. F., & Chan, J. C. L. (2014). Impacts of initial vortex size and planetary vorticity on tropical cyclone size. *Quarterly Journal of the Royal Meteorological Society*, *140*(684), 2235–2248. https://doi.org/10.1002/qj.2292

Charnock, H. (1955). Wind stress on a water surface. *Quarterly Journal of the Royal Meteorological Society*, *81*(350), 639–640. https://doi.org/10.1002/qj.49708135027

Chassignet, E., Hurlburt, H., Metzger, E. J., Smedstad, O., Cummings, J., Halliwell, G., et al. (2009). US GODAE: Global Ocean Prediction with the HYbrid Coordinate Ocean Model (HYCOM). *Oceanography*, *22*(2), 64–75. https://doi.org/10.5670/oceanog.2009.39

Chen, F., & Dudhia, J. (2001). Coupling an Advanced Land Surface-Hydrology Model with the Penn State-NCAR MM5 Modeling System. Part I: Model Implementation and Sensitivity. *Monthly Weather Review*, *129*(4), 569–585. https://doi.org/10.1175/1520-0493(2001)129<0569:caalsh>2.0.co;2

Chen, S. S., Price, J. F., Zhao, W., Donelan, M. A., & Walsh, E. J. (2007). The CBLAST-Hurricane Program and the Next-Generation Fully Coupled Atmosphere-Wave-Ocean Models for Hurricane Research and Prediction. *Bulletin of the American Meteorological Society*, *88*(3), 311–318. https://doi.org/10.1175/bams-88-3-311

Cummings, J. A., & Smedstad, O. M. (2013). Variational data Assimilation for the Global Ocean. In S. K. Park & L. Xu (Eds.). 303–343. *Data Assimilation for Atmospheric, Oceanic and Hydrologic Applications*. Springer Berlin Heidelberg. https://doi.org/10.1007/978-3-642-35088-7_13

Curcic, M., Chen, S. S., & Özgökmen, T. M. (2016). Hurricane-induced ocean waves and stokes drift and their impacts on surface transport and dispersion in the Gulf of Mexico. *Geophysical Research Letters*, *43*(6), 2773–2781. https://doi.org/10.1002/2015gl067619

Dai, D., Qiao, F., Sulisz, W., Han, L., & Babanin, A. (2010). An experiment on the nonbreaking surface-wave-induced vertical mixing. *Journal of Physical Oceanography*, *40*(9), 2180–2188. https://doi.org/10.1175/2010jpo4378.1

DeMaria, M., Sampson, C. R., Knaff, J. A., & Musgrave, K. D. (2014). Is tropical cyclone intensity guidance improving? *Bulletin of the American Meteorological Society*, *95*(3), 387–398. https://doi.org/10.1175/bams-d-12-00240.1

Doyle, J., Hodur, R., Chen, S., Jin, Y., Msokaitis, J., Wang, S., et al. (2014). Tropical Cyclone Prediction Using COAMPS-TC. *Oceanography*, *27*(3), 104–115. https://doi.org/10.5670/oceanog.2014.72

Dudhia, J. (1989). Numerical study of convection observed during the winter monsoon experiment using a mesoscale two-dimensional model. *Journal of the Atmospheric Sciences*, *46*(20), 3077–3107. https://doi.org/10.1175/1520-0469(1989)046<3077:nsocod>2.0.co;2

Dvorak, V. F. (1975). Tropical cyclone intensity analysis and forecasting from satellite imagery. *Monthly Weather Review*, *103*(5), 420–430. https://doi.org/10.1175/1520-0493(1975)103<0420:tciaaf>2.0.co;2

Emanuel, K. A. (1986). An air-sea interaction theory for tropical cyclones. Part I: Steady-state maintenance. *Journal of the Atmospheric Sciences*, *43*(6), 585–605. https://doi.org/10.1175/1520-0469(1986)043<0585:aasitf>2.0.co;2

Fairall, C. W., Banner, M. L., Peirson, W. L., Asher, W., & Morison, R. P. (2009). Investigation of the physical scaling of sea spray spume droplet production. *Journal of Geophysical Research*, *114*(C10). https://doi.org/10.1029/2008jc004918

Fairall, C. W., Bradley, E. F., Hare, J. E., Grachev, A. A., & Edson, J. B. (2003). Bulk Parameterization of Air-Sea Fluxes: Updates and Verification for the COARE Algorithm. *Journal of Climate*, *16*(4), 571–591. https://doi.org/10.1175/1520-0442(2003)016<0571:bpoasf>2.0.co;2

Fairall, C. W., Bradley, E. F., Rogers, D. P., Edson, J. B., & Young, G. S. (1996). Bulk parameterization of air-sea fluxes for Tropical Ocean-Global Atmosphere Coupled-Ocean Atmosphere Response Experiment. *Journal of Geophysical Research*, *101*(C2), 3747–3764. https://doi.org/10.1029/95jc03205

Garg, N., Ng, E. Y. K., & Narasimalu, S. (2018). The effects of sea spray and atmosphere-wave coupling on air-sea exchange during a tropical cyclone. *Atmospheric Chemistry and Physics*, *18*(8), 6001–6021. https://doi.org/10.5194/acp-18-6001-2018

Hasselmann, D. E., Dunckel, M., & Ewing, J. A. (1980). Directional wave spectra observed during JONSWAP 1973. *Journal of Physical Oceanography*, *10*(8), 1264–1280. https://doi.org/10.1175/1520-0485(1980)010<1264:dwsodj>2.0.co;2

Hersbach, H., Bell, B., Berrisford, P., Hirahara, S., Horányi, A., Muñoz-Sabater, J., et al. (2020). The ERA5 global reanalysis. *Quarterly Journal of the Royal Meteorological Society*, *146*(730), 1999–2049. https://doi.org/10.1002/qj.3803

Hoarau, T., Barthe, C., Tulet, P., Claeys, M., Pinty, J. P., Bousquet, O., et al. (2018). Impact of the generation and activation of sea salt aerosols on the evolution of tropical cyclone dumile. *Journal of Geophysical Research: Atmospheres*, *123*(16), 8813–8831. https://doi.org/10.1029/2017jd028125

Hong, S.-Y., Juang, H.-M. H., & Zhao, Q. (1998). Implementation of Prognostic Cloud Scheme for a Regional Spectral Model. *Monthly Weather Review*, *126*(10), 2621–2639. https://doi.org/10.1175/1520-0493(1998)126<2621:iopcsf>2.0.co;2

Janssen, P. A. E. M. (1989). Wave-Induced Stress and the drag of Air Flow over Sea Waves. *Journal of Physical Oceanography*, *19*(6), 745–754. https://doi.org/10.1175/1520-0485(1989)019<0745:wisatd>2.0.co;2

Janssen, P. A. E. M. (1991). Quasi-linear theory of wind-wave generation applied to wave forecasting. *Journal of Physical Oceanography*, *21*(11), 1631–1642. https://doi.org/10.1175/1520-0485(1991)021<1631:qltoww>2.0.co;2
Kain, J. S., & Fritsch, J. M. (1990). A one-dimensional entraining/detraining plume model and its application in convective parameterization. *Journal of the Atmospheric Sciences*, *47*(23), 2784–2802. https://doi.org/10.1175/1520-0469(1990)047<2784:aodepm>2.0.co;2
Li, Y., Peng, S., Wang, J., & Yan, J. (2014). Impacts of nonbreaking wave-stirring-induced mixing on the upper ocean thermal structure and typhoon intensity in the South China Sea. *Journal of Geophysical Research: Oceans*, *119*(8), 5052–5070. https://doi.org/10.1002/2014jc009956
Lin, Y.-L., Farley, R. D., & Orville, H. D. (1983). Bulk parameterization of the snow field in a cloud model. *Journal of Climate and Applied Meteorology*, *22*(6), 1065–1092. https://doi.org/10.1175/1520-0450(1983)022<1065:bpotsf>2.0.co;2
Liu, B., Liu, H., Xie, L., Guan, C., & Zhao, D. (2011). A coupled atmosphere-wave-ocean modeling system: Simulation of the intensity of an idealized tropical cyclone. *Monthly Weather Review*, *139*(1), 132–152. https://doi.org/10.1175/2010mwr3396.1
Liu, J., Curry, J. A., Clayson, C. A., & Bourassa, M. A. (2011). High-resolution satellite surface latent heat fluxes in north atlantic hurricanes. *Monthly Weather Review*, *139*(9), 2735–2747. https://doi.org/10.1175/2011mwr3548.1
Liu, L., Li, R., Zhang, C., Yang, G., Wang, B., & Dong, L. (2015). Enhancement for bitwise identical reproducibility of Earth system modeling on the C-Coupler platform. *Geoscientific Model Development Discussions*, 2403–2435.
Liu, L., Yang, G., Wang, B., Zhang, C., Li, R., Zhang, Z., et al. (2014). C-Coupler1: A Chinese community coupler for Earth system modeling. *Geoscientific Model Development*, *7*(5), 2281–2302. https://doi.org/10.5194/gmd-7-2281-2014
Liu, L., Zhang, C., Li, R., Wang, B., & Yang, G. (2018). C-Coupler2: A flexible and user-friendly community coupler for model coupling and nesting. *Geoscientific Model Development*, *11*(9), 3557–3586. https://doi.org/10.5194/gmd-11-3557-2018
Magnusson, L., Bidlot, J. R., Bonavita, M., Brown, A. R., Browne, P. A., De Chiara, G., et al. (2019). ECMWF Activities for Improved Hurricane Forecasts. *Bulletin of the American Meteorological Society*, *100*(3), 445–458. https://doi.org/10.1175/bams-d-18-0044.1
Mehra, A., Tallapragada, V., Zhang, Z., Liu, B., Zhu, L., Wang, W., & Kim, H.-S. (2018). Advancing the state of the art in operational tropical cyclone forecasting at Ncep. *Tropical Cyclone Research and Review*, *7*(1), 51–56.
Mellor, G. L., & Yamada, T. (1982). Development of a turbulence closure model for geophysical fluid problems. *Reviews of Geophysics*, *20*(4), 851–875. https://doi.org/10.1029/RG020i004p00851
Mlawer, E. J., Taubman, S. J., Brown, P. D., Iacono, M. J., & Clough, S. A. (1997). Radiative transfer for inhomogeneous atmospheres: RRTM, a validated correlated-k model for the longwave. *Journal of Geophysical Research*, *102*(D14), 16663–16682. https://doi.org/10.1029/97JD00237
Mogensen, K. S., Magnusson, L., & Bidlot, J.-R. (2017). Tropical cyclone sensitivity to ocean coupling in the ECMWF coupled model. *Journal of Geophysical Research: Oceans*, *122*(5), 4392–4412. https://doi.org/10.1002/2017jc012753
Montgomery, M. T., & Smith, R. K. (2014). Paradigms for tropical cyclone intensification. *Australian Meteorological and Oceanographic Journal*, *64*, 37–66. https://doi.org/10.22499/2.6401.005
Moon, I.-J., Ginis, I., Hara, T., & Thomas, B. (2007). A physics-based parameterization of air-sea momentum flux at high wind speeds and its impact on hurricane intensity predictions. *Monthly Weather Review*, *135*(8), 2869–2878. https://doi.org/10.1175/mwr3432.1
Olabarrieta, M., Warner, J. C., Armstrong, B., Zambon, J. B., & He, R. (2012). Ocean-atmosphere dynamics during Hurricane Ida and Nor'Ida: An application of the coupled ocean-atmosphere-wave-sediment transport (COAWST) modeling system. *Ocean Modelling*, *43–44*, 112–137. https://doi.org/10.1016/j.ocemod.2011.12.008
Perrie, W., Zhang, W., Andreas, E. L., Li, W., Gyakum, J., & McTaggart-Cowan, R. (2005). Sea spray impacts on intensifying midlatitude cyclones. *Journal of the Atmospheric Sciences*, *62*(6), 1867–1883. https://doi.org/10.1175/jas3436.1
Pianezze, J., Barthe, C., Bielli, S., Tulet, P., Jullien, S., Cambon, G., et al. (2018). A new coupled ocean-waves-atmosphere model designed for tropical storm studies: Example of Tropical Cyclone Bejisa (2013-2014) in the South-West Indian Ocean. *Journal of Advances in Modeling Earth Systems*, *10*(3), 801–825. https://doi.org/10.1002/2017ms001177
Powell, M. D., Vickery, P. J., & Reinhold, T. A. (2003). Reduced drag coefficient for high wind speeds in tropical cyclones. *Nature*, *422*(6929), 279–283. https://doi.org/10.1038/nature01481
Price, J. F. (1981). Upper Ocean Response to a Hurricane. *Journal of Physical Oceanography*, *11*(2), 153–175. https://doi.org/10.1175/1520-0485(1981)011<0153:uortah>2.0.co;2. https://journals.ametsoc.org/view/journals/phoc/11/2/1520-0485_1981_011_0153_uortah_2_0_co_2.xml
Qiao, F., Yuan, Y., Ezer, T., Xia, C., Yang, Y., Lü, X., & Song, Z. (2010). A three-dimensional surface wave–ocean circulation coupled model and its initial testing. *Ocean Dynamics*, *60*(5), 1339–1355. https://doi.org/10.1007/s10236-010-0326-y
Qiao, F., Yuan, Y., Yang, Y., Zheng, Q., Xia, C., & Ma, J. (2004). Wave-induced mixing in the upper ocean: Distribution and application to a global ocean circulation model. *Geophysical Research Letters*, *31*(11). https://doi.org/10.1029/2004gl019824
Rappaport, E. N., Franklin, J. L., Avila, L. A., Baig, S. R., Beven, J. L., Blake, E. S., et al. (2009). Advances and Challenges at the National Hurricane Center. *Weather and Forecasting*, *24*(2), 395–419. https://doi.org/10.1175/2008waf2222128.1
Renault, L., & Marchesiello, P. (2022). Ocean tides can drag the atmosphere and cause tidal winds over broad continental shelves. *Communications Earth & Environment*, *3*(1), 70. https://doi.org/10.1038/s43247-022-00403-y
Renault, L., Molemaker, M. J., Gula, J., Masson, S., & McWilliams, J. C. (2016). Control and Stabilization of the Gulf Stream by Oceanic Current Interaction with the Atmosphere. *Journal of Physical Oceanography*, *46*(11), 3439–3453. https://doi.org/10.1175/jpo-d-16-0115.1
Scharroo, R., Leuliette, E., Lillibridge, J., Byrne, D., Naeije, M., & Mitchum, G. (2013). RADS: Consistent multi-mission products.
Skamarock, W. C., Klemp, J. B., Dudhia, J., Gill, D. O., Barker, D., Duda, M. G., et al. (2008). *A Description of the Advanced Research WRF Version 3 (No. NCAR/TN-475+STR)*. University Corporation for Atmospheric Research. https://doi.org/10.5065/D68S4MVH
Smith, R. K., Montgomery, M. T., & Van Sang, N. (2009). Tropical cyclone spin-up revisited. *Quarterly Journal of the Royal Meteorological Society*, *135*(642), 1321–1335. https://doi.org/10.1002/qj.428
Uhlhorn, E. W., & Black, P. G. (2003). Verification of remotely sensed sea surface winds in hurricanes. *Journal of Atmospheric and Oceanic Technology*, *20*(1), 99–116. https://doi.org/10.1175/1520-0426(2003)020<0099:vorsss>2.0.co;2
Wada, A., Kanada, S., & Yamada, H. (2018). Effect of air-sea environmental conditions and interfacial processes on extremely intense Typhoon Haiyan (2013). *Journal of Geophysical Research: Atmospheres*, *123*(18). https://doi.org/10.1029/2017jd028139
Wang, G., Qiao, F., & Xia, C. (2010). Parallelization of a coupled wave-circulation model and its application. *Ocean Dynamics*, *60*(2), 331–339. https://doi.org/10.1007/s10236-010-0274-6
Wang, G., Zhao, B., Qiao, F., & Zhao, C. (2018). Rapid intensification of Super Typhoon Haiyan: The important role of a warm-core ocean eddy. *Ocean Dynamics*, *68*(12), 1649–1661. https://doi.org/10.1007/s10236-018-1217-x
Warner, J. C., Armstrong, B., He, R., & Zambon, J. B. (2010). Development of a Coupled Ocean-Atmosphere-Wave-Sediment Transport (COAWST) Modeling System. *Ocean Modelling*, *35*(3), 230–244. https://doi.org/10.1016/j.ocemod.2010.07.010
Xie, L., Bin, L., Huiqing, L., & Changlong, G. (2010). Numerical simulation of tropical cyclone intensity using an air-sea coupled prediction system. *Advances in Geosciences*, *18*, 19–43.

Xu, J., & Wang, Y. (2010). Sensitivity of the simulated tropical cyclone inner-core size to the initial vortex size. *Monthly Weather Review*, *138*(11), 4135–4157. https://doi.org/10.1175/2010mwr3335.1

Yamaguchi, M., Ishida, J., Sato, H., & Nakagawa, M. (2017). WGNE intercomparison of tropical cyclone forecasts by operational nwp models: A quarter century and beyond. *Bulletin of the American Meteorological Society*, *98*(11), 2337–2349. https://doi.org/10.1175/bams-d-16-0133.1

Yang, Y. Z., Qiao, F., Zhao, W., Teng, Y., & Yuan, Y. (2005). MASNUM ocean wave numerical model in spherical coordinates and its application. *Acta Oceanologica Sinica*, *27*(2), 7.

Yu, H., Chen, P., Li, Q., & Tang, B. (2013). Current capability of operational numerical models in predicting tropical cyclone intensity in the Western North Pacific. *Weather and Forecasting*, *28*(2), 353–367. https://doi.org/10.1175/waf-d-11-00100.1

Yuan, Y., Hua, F., Pan, Z., & Sun, L. (1991). LAGFD-WAM numerical wave model-?. Basic physical model, 483–488.

Yuan, Y., Hua, F., Pan, Z., & Sun, L. (1992). LAGFD-WAM numerical wave model-II. Characteristics inlaid scheme and its application. *Acta Oceanologica Sinica*(01), 13–23.

Zhang, H., Chen, D., Zhou, L., Liu, X., Ding, T., & Zhou, B. (2016). Upper ocean response to typhoon Kalmaegi (2014). *Journal of Geophysical Research: Oceans*, *121*(8), 6520–6535. https://doi.org/10.1002/2016jc012064

Zhang, J. A., Gopalakrishnan, S., Marks, F. D., Rogers, R. F., & Tallapragada, V. (2012). A developmental Framework for Improving Hurricane Model Physical Parameterizations Using Aircraft Observations. *Tropical Cyclone Research and Review*, *1*(4), 419–429.

Zhang, J. A., & Marks, F. D. (2015). Effects of Horizontal diffusion on Tropical Cyclone Intensity Change and Structure in Idealized Three-dimensional Numerical Simulations. *Monthly Weather Review*, *143*(10), 3981–3995. https://doi.org/10.1175/mwr-d-14-00341.1

Zhang, J. A., Marks, F. D., Sippel, J. A., Rogers, R. F., Zhang, X., Gopalakrishnan, S. G., et al. (2018). Evaluating the impact of improvement in the horizontal diffusion parameterization on hurricane prediction in the operational Hurricane Weather Research and Forecast (HWRF) Model. *Weather and Forecasting*, *33*(1), 317–329. https://doi.org/10.1175/waf-d-17-0097.1

Zhang, J. A., Nolan, D. S., Rogers, R. F., & Tallapragada, V. (2015). Evaluating the impact of improvements in the boundary layer parameterization on hurricane intensity and structure forecasts in HWRF. *Monthly Weather Review*, *143*(8), 3136–3155. https://doi.org/10.1175/mwr-d-14-00339.1

Zhang, J. A., & Rogers, R. F. (2019). Effects of parameterized boundary layer structure on hurricane rapid intensification in shear. *Monthly Weather Review*, *147*(3), 853–871. https://doi.org/10.1175/mwr-d-18-0010.1

Zhang, J. A., Rogers, R. F., & Tallapragada, V. (2017). Impact of parameterized boundary layer structure on tropical cyclone rapid intensification forecasts in HWRF. *Monthly Weather Review*, *145*(4), 1413–1426. https://doi.org/10.1175/mwr-d-16-0129.1

Zhao, B., Qiao, F., Cavaleri, L., Wang, G., Bertotti, L., & Liu, L. (2017). Sensitivity of typhoon modeling to surface waves and rainfall. *Journal of Geophysical Research: Oceans*, *122*(3), 1702–1723. https://doi.org/10.1002/2016jc012262

Zweers, N. C., Makin, V. K., Vries, J. W., & Kudryavtsev, V. N. (2015). The impact of spray-mediated enhanced enthalpy and reduced drag coefficients in the modelling of tropical cyclones. *Boundary-Layer Meteorology*, *155*(3), 501–514. https://doi.org/10.1007/s10546-014-9996-1